UNITED STATES

DEPARTMENT OF THE INTERIOR
GEOLOGICAL SURVEY

INTERAGENCY REPORT NASA-82

THERMAL ANOMALIES AND GEOLOGIC FEATURES OF THE MONO LAKE AREA, CALIFORNIA, AS REVEALED BY INFRARED IMAGERY *

by

Jules D. Friedman **

68-107

Prepared by the Geological Survey
for the National Aeronautics and
Space Administration (NASA)

*Work performed under NASA Contract No. R-146-09-020 and Work Order No. T-65754-G
**U.S. Geological Survey, Washington, D.C.

CONTENTS

	Page
Abstract	1
Introduction	2
Previous Investigations	3
Objectives	4
Procedures	4
Symbols and Abbreviations	7
Geology of Mono Lake and Craters Area	9
Lunar Analogues	11
Geologic Factors Affecting Infrared Image Tonal Density	11
Radiative heat transfer	11
Convective heat transfer	20
Other anomalies	22
Summary	22
Footnotes	26
Illustrations	27
Plates	31
Figures	38
Tables	67
Acknowledgements	82
References	83

ILLUSTRATIONS

Plates

Plate		Page
1	- Geologic map of the Mono Craters Area, California with accompanying explanation.	31
2A-F	- Infrared imagery of Black Point, Mono Lake, at 4-hour intervals, July 27-28, 1966.	32
3A-F	- Infrared imagery of Paoha Island, Mono Lake, at 4-hour intervals, July 27-28, 1966.	33
4A-F	- Infrared imagery of Aeolian Buttes at 4-hour intervals, July 27-28, 1966.	34
5A-F	- Infrared imagery of North Coulee, at 4-hour intervals, July 27-28, 1966.	35
6A-B	- Infrared imagery of the main rhyolite-obsidian complex at Mono Craters, 0800 hours, June 4, 1965.	36
7	- Photographs of a) thermal spring deposits, b) recent andesite-basalt volcanics, c) structural deformation of wavecut bench, and d) crater morphology of Paoha and Negit Islands.	37

FIGURES

Figure		Page
1.	Flightline, Mono Craters test site, California.	38
2.	Isodensity scan of IR imagery, Wilson Creek delta and escarpment, Black Point, 0750, 7/27/66.	39
3.	Isodensity scan of IR imagery, Wilson Creek delta and escarpment, Black Point, 1233. 7/27/66.	40
4.	Isodensity scan of IR imagery, Wilson Creek delta and escarpment, Black Point, 1631, 7/27/66.	41
5.	Isodensity scan of IR imagery, Wilson Creek delta and escarpment, Black Point, 2008, 7/27/66.	42
6.	Isodensity scan of IR imagery, Wilson Creek delta and escarpment, Black Point, 2359, 7/27/66.	43
7.	Isodensity scan of IR imagery, Wilson Creek delta and escarpment, Black Point, 0404, 7/28/66.	44
8.	Isodensity scan of IR imagery, Deschambeau Ranch, Black Point, Mono Lake, 2359, 7/27/66.	45
9.	Isodensity scan of IR imagery, NE Paoha Island, Mono Lake, 2010, 7/27/66.	46
10.	Isodensity scan of IR imagery, NE Paoha Island, Mono Lake, 2038, 7/27/66.	47
11.	Isodensity scan of IR imagery, NE Paoha Island, Mono Lake, 0407, 7/28/66.	48
12.	Isodensity scan of IR imagery showing area of thermal anomalies, eastern Paoha Island, Mono Lake, 2010, 7/27/66.	49

Page

13. Isodensity scan of IR imagery showing area of thermal anomalies in detail, eastern Paoha Island, Mono Lake, 2038, 7/27/66. 50

14A. Incident radiant solar flux Mono Lake, July 27 and 28, 1966 51

14B. Surface temperatures, Mono Instrument Stations, July 27 and 28, 1966. 52

15. Surface radiant temperatures, Aeolian Buttes, Mono area, July 27-28, 1966. 53

16. Surface and near-surface temperatures, Mono South Beach station, July 27-28, 1966. 54

17. Change in temperature with depth, East Pumice Sand Flat, Mono Area, July 27-28, 1966. 55

18. Surface temperature of Mono Lake, South Beach area, July 27-28, 1966. 56

19. IR image density in relation to surface temperature, Black Point, Mono Lake, July 27-28, 1966. 67

20. Change in relative film density with time during a diurnal cycle for three lithologies and water, Black Point, July 27-28, 1966. 58

21. Graph of $f(L, \delta, \omega, t)$ for a diurnal cycle at the summer solstice, autumnal equionox and July 27-28, 1966, for latitude 38°N. 59

22. Recorded variations in apparent surface temperature with time during period of infrared survey, Black Point, for two lithologies, July 27-28, 1966. 60

23. Theoretical diurnal surface temperature variations for two lithologies at Black Point, July 27-28, 1966. 61

TABLES

Table		Page
1.	Infrared flight log, July 27-28, 1966, Mono Craters Area.	67
2.	Time-rate of change of image tonal density during a diurnal cycle, Mono Area, July 27-28, 1966.	68
3.	Integrated 8-14μ emissivities (ϵ) of rocks from Mono Craters region.	69
4.	Relationship between amplitude of diurnal surface temperature curves and thermal parameters for selected lithologies of the Mono Area, July 27-28, 1966.	70

Page

24. Recorded variation in blackbody-equivalent surface temperature with time during period of infrared survey, Aeolian Buttes, July 27-28, 1966. 62

25. Theoretical variations in surface temperatures of two lithologies at Aeolian Buttes, July 27-28, 1966. 63

26. Change in apparent emissivity (ε_c) as a function of cavity shape and integrated emissivity ($\varepsilon_{\lambda 8\text{-}14\mu}$) of the cavity wall. 64

27. Aerial photograph of Paoha Island showing areas scanned by isodensitracer technique. 65

28. Subsided Santorin (Thíra) caldera in the Cyclades archipelago, Aegean Sea. 66

THERMAL ANOMALIES AND GEOLOGIC FEATURES OF THE MONO LAKE AREA, CALIFORNIA, AS REVEALED BY INFRARED IMAGERY

by

Jules D. Friedman

ABSTRACT

The Mono Lake area, California, was selected for airborne infrared scanning radiometer experiments because of the exposure in this area of a variety of lithologies having different physical and thermal properties as well as a diversity of textural and morphologic features. Infrared surveys were undertaken in 1965 and 1966 to measure variations in infrared emission from the surface in the 4.5 - 5.5μ and 8-14μ bands. Areal variations in emission from the surface were registered on film as differences in image tonal density. In addition, variations of surface radiant temperature with time during the diurnal cycle were recorded at several selected localities. The contrasting thermal patterns observed can be grouped as follows:

1) Thermal anomalies due to convective heat loss detected when the temperature difference between the heat source and surrounding terrain was maximal, e.g., hot springs and a warm effluent at Black Point.

2) Daytime radiant-temperature differences resulting from variations in the incident radiant solar flux as a function of microrelief and morphology of the surface.

3) Nighttime radiant-temperature differences resulting from contrasts in physical and thermal properties of various lithologic units and water expressed as different rates of change in emission, e.g., between olivine basalt lapilli-ash beach deposits, lacustrine carbonate deposits and water along the north shore of Mono Lake at Black Point.

The detectability of the third group of thermal patterns in the Mono Lake area is of the greatest experimental interest. Nighttime radiative heat loss is dependent upon the $\left(\frac{1-\alpha_o}{\beta}\right)$ ratio as a property of materials,

the total radiant energy incident on the surface during daytime (J_o as a function of topography) and integrated emissivity (ϵ) as a function of surface roughness and blackbody cone effects, and to a lesser extent, of composition.

INTRODUCTION

Infrared airborne surveys of the Mono area were undertaken in 1965 and 1966 utilizing a NASA Convair 240 and USGS twin-engine Beechcraft to study natural thermal anomalies related to structure and to analyze emittance characteristics of several lithologies as represented on infrared imagery. Imagery taken in 1965 using a detector sensitive to radiation in the 4.5 - 5.5μ wavelength band is not analyzed in detail in the present report, but was used to plan the 1966 surveys. Variations in radiant emission from the earth's surface in the 8-14μ wavelength interval were registered during a diurnal cycle as image tonal density differences on conventional photographic film by an airbrone scanning radiometer on July 27-28, 1966. In addition to earlier overflights and several test runs, three N-S flightlines (Figure 1) with a total flight length of 54 miles were flown during a sequence of six surveys (Table 1) during a 24-hour period in the Mono area, July 26-28, 1966. Ground monitoring stations at Black Point, South Beach, Mono Lake and Aeolian Buttes, utilizing automatic recording, variable-sequencer thermistor and infrared radiometer systems, recorded ground surface temperatures in a variety of materials simultaneously with overflights. This report is primarily a summary of the data obtained from the July 27-28, 1966, experiment. At an earlier stage in the project, a geologic map (Plate 1), was compiled at a scale of 1:31,680 on a rectified orthophotomosaic base to provide geologic control for location of ground monitoring stations, sample collection and interpretation of the infrared imagery acquired.

The unusual variety of lithologic, volcanic and tectonic features of Mono Basin, the locus of the most intense and complex volcanism of the Owens Valley region, influenced selection of this area for the infrared survey experiment. Lithologies surveyed include late Pleistocene olivine basalt pyroclastics of the sublacustrine Black Point volcano, recent andesite-basalt [1] volcanics and carapace of lacustrine deposits of Negit and Paoha Island, the largely recent rhyolite-obsidian complex of brecciated youthful tholoids, coulees and block craters; as well as rhyolitic tephra rings, ramparts and basin-floor layers of the main crater complex south of the lake, and the older Pleistocene Bishop tuff of Aeolian Buttes.

Previous Investigations

The Mono Lake - Mono Craters area has been studied extensively during the past eighty years with attention focused primarily on the geology of the Lake Basin and the volcanic rhyolite-obsidian complex. For a list of selected reports on the geology of the area through 1965, see Friedman, 1966, Geologic Map of the Mono Craters Area, California, U. S. Geol. Survey Technical Letter NASA-12. The geologic map compilation prepared for Technical Letter NASA-12 (reproduced in this report on Plate 1) sums up much of the literature for the specific area of infrared radiometry surveys reported in this Technical Letter. The most recently published geological map of a large part of the area is Kistler, 1966, Geological Map of the Mono Craters Quadrangle, Mono and Toulumne Counties, California, U. S. Geol. Survey Geological Quadrangle Map GQ-462.

Previous studies of the Mono area carried out by the Infrared Laboratory, U.S. Geological Survey, include Daniels, 1966, Infrared Spectral Emittance of Rocks from the Pisgah Crater and Mono Craters Areas, California, U.S. Geol. Survey Technical Letter NASA-13, in which the spectral emittance in the 8-14μ wavelength band, of selected rock types from the Mono area is reported. Daniels concluded that the emittance spectra of acidic igneous rocks of the area are very similar, are recognizable in spite of their rough and weathered surfaces but differ from the spectra of basaltic rocks from the area.[2]

Objectives

The purpose of the Mono area infrared imagery experiment reported here is to determine the degree to which it is possible to distinguish lithologic and other natural materials of different thermal properties or different emissivity (ϵ) by means of infrared emission variations resulting from varying rates of cooling or warming at sunset and dawn and registered by tonal density differences on photographic film by an airborne scanning radiometer that senses radiation in the 8-14μ wavelength band from the terrestrial surface.

Procedures

Three north-south flightlines (Figure 1) were used to control the infrared surveys made with a Reconofax IV scanner mounted in the Geological Survey's twin-engine Beechcraft on July 27-28, 1966. Rotating high-intensity beacons marked the flightlines during night surveys. Several ground instrument monitoring stations were set up along or close to the flightlines at geologic contacts between selected lithologic map units: See Table 1. The ground stations were designed to obtain observations on

diurnal temperature variations of selected natural lithologic surfaces. Two types of instrument systems were operated simultaneously with survey overflights: Barnes IT-3 and IT-2 fixed-field radiometers recording continuously on an Esterline-Angus strip-chart recorder and Sprinkle variable-sequencer thermistor-probe systems also recording on Esterline-Angus recorders. Other equipment included automatic recording tempscribe thermographs and a recording Epply pyrheliometer to determine variations in the incident radiant flux at the terrestrial surface,[3] recording thermographs for determining ambient temperature variations and a velometer for near-surface wind variations. Diurnal surface-temperature curves were established from these ground measurements.

Infrared survey overflights were made at 4-hour intervals during a 24-hour cycle. Selected frames of infrared imagery obtained by this method were scanned in the laboratory at magnifications of five and ten times by a double-beam recording isodensitomer to obtain color printouts of film emulsion density increments -- roughly equivalent to form-line isoradiance maps with a variable contour interval. Density profiles were also obtained. A comparison between image tonal density differences and diurnal surface-temperature curves for various materials established from ground observations (Figures 14-18) was the next step. Thermal properties and infrared integrated bandpass emissivity determinations on rocks of the Mono area were compiled to aid in construction of theoretical diurnal surface-temperature curves

---

[3] The major part of the incident radiant solar flux is recorded by the Epply pyrheliometer. The transmission capability of the glass bulb is above 50 percent for wavelengths from 305Å to 4.4μ and is above 90 percent for wavelengths between 360Å and 2.6μ.

using equations for a physical model. The theoretical warming and cooling curves obtained were compared with those obtained by ground observation to estimate the degree to which surface temperature variations and infrared emission variations are influenced by differences in the thermal inertia (β) of natural materials. Finally, anomalous thermal patterns recorded on the infrared imagery, but not attributable to insolation variations, thermal-parameter, or emissivity differences of materials, were interpreted geologically.

Accuracy of Surface Temperature Measurements
At Ground Monitoring Stations

Barnes IT-3 Infrared Thermometer (Fixed-Field Radiometer). Integrates temperatures over the entire area subtended by its optical system. Absolute accuracy attainable within 1.2°C for a target of unity emissivity. Average emissivity of surfaces studied is 0.9±. Additional error of $<1^{\circ}$C inherent in Esterline-Angus recording system.

Sprinkle Variable Sequencer Multiprobe Thermistor System. Error less than 1°C, but subject to additional error of $<.1^{\circ}$C inherent in Esterline-Angus recording system.

Tempscribe Recording Thermograph. Calibration error of less than 1°C, but additional error introduced in positioning needle arm.

SYMBOLS AND ABBREVIATIONS

α = Thermal diffusivity in cm^2 sec^{-1}.

AGC = Automatic gain control setting of scanning radiometer.

β = Thermal inertia, i.e., measure of the rate of heat transfer at the interface between two dissimilar media in cal cm^{-2} $^oC^{-1}$ $sec^{-1/2}$.

C = Specific heat in cal gm C^{o-1}.

$B(\lambda, T)$ = The amount of energy radiated in all directions from one cm^2 blackbody surface at temperature T per second and per unit wavelength interval.

ϵ = Integrated emissivity; in this report the ratio $I_{N/}I_{BB}$ determined in the laboratory for a flat surface for the 8-14μ wavelength interval.

ϵ_c = Apparent emissivity dependent upon cavity shape.

ϵ_λ = Spectral emissivity.

F_o = Net radiant solar flux, measured as the diurnal maximum incident radiant flux (J_o) minus the reflected radiant flux (R_o).

F_o/β = Net radiant solar flux - thermal inertia ratio that controls the initial temperature rise of a point on the terrestrial surface; approximately proportional to the maximum-minimum amplitude of a diurnal surface temperature curve.

γ = Film emulsion density as measured by double-beam recording isodensitometer.

$\Delta\gamma$ = Increment in film density; in a specific frame of infrared imagery a function of infrared emission from the terrestrial surface.

I_{BB} = Intensity of radiation emitted by one cm^2 of a natural surface within a specific wavelength range, per second, at blackbody-equivalent temperature T.

I_N = Radiation emitted by one cm^2 of a natural surface within a specific wavelength range, per second, at temperature T.

J_o = Incident radiant flux at the terrestrial surface.

k = Thermal conductivity in cal cm^{-1} sec^{-1} $^oC^{-1}$.

Ka = Quartz monzonite of Cretaceous age of Aeolian Buttes. See Plate 1, Geologic Map of Mono Craters Area, California.

λ = Wavelength; measured in microns (μ) in the infrared region of the electromagnetic spectrum.

L = In Equations (4) and (5), latitude.

μ = Micron; one millionth of a meter.

N = Radiance in watts cm^{-2} $ster^{-1}$.

ω = The angular velocity of the earth, 7.27×10^{-5} radians sec^{-1}.

Q = Quaternary geologic map units representing distinctive lithologies; subscripts indicate specific map units - see Explanation accompanying Plate 1, Geologic Map of the Mono Craters Area, California.

ρ = In this report, bulk density in gm cm^{-3}.

r_o = Total reflectivity of a surface for the incident radiation J_o; $r_o = \frac{R_o}{J_o}$; $\frac{(1-r_o)}{\beta}$ = ratio of total absorptivity to thermal inertia of a specific material; characteristic of specific lithologies.

R_o = Reflected radiant solar flux.

δ = Solar declination.

T = Temperature in degrees Centigrade or Kelvin.

Tmd = Mean daily surface temperature of a specific point on the terrestrial surface.

T_o = Surface temperature of a specific point on the terrestrial surface at a given instant in time.

t = Time in Equation (4) measured from local noon.

$V/_H$ = Ratio of velocity of survey aircraft to altitude; if aircraft velocity and film transport are improperly synchronized $V/_H$ settings of scanning radiometer may cause geometric distortion of infrared imagery.

Geology of Mono Lake and Craters Area

The volcanotectonic depression containing Mono Lake has been the locus of the greatest concentration of volcanic activity in the upper Owens Valley since the mid-Pliocene. The oldest manifestations of volcanism in the area are the Tertiary volcanic rocks of the Bodie area north of Mono Lake. Rhyolitic ignimbrite of the Bishop tuff of Pleistocene age is exposed in the Aeolian Buttes area several miles south of the lake. The volcanotectonic basin has undergone continued subsidence throughout Quaternary time. It is bounded by near-vertical faults on the basis of recent geophysical studies (Pakiser and others, 1960, 1964) and probably contains about 300 cubic miles of Cenozoic sediments and volcanics to a depth of approximately 18,000 feet. Mono Lake itself presently occupies the lowest part of the basin. The surface of the remainder of the basin is underlain by lacustrine deposits covered in part by ashfall tephra deposits. Studies of the lake bottom topography (Scholl and others, 1965) indicate that its eastern half is a smooth plain, but the western half has two deep basins with irregular topography attributed to faulting, volcanism, glaciation and submarine slumping. Paoha and Negit Islands in the lake are of volcanic origin and represent some of the most recent volcanic activity in the area.

A gravity low with a Bouguer gravity value of about — 260 mgals is centered on Paoha Island. (Pakiser and others, 1960). Slump features in Recent marl deposits exposed on Paoha Island may be the surface expression of sublacustrine uplift or volcanism. East of Negit Island is an archipelago of eight small islands composed of lacustrine sediments; some of these islands are diked and silled with andesitic lava (Scholl and others, 1966). Black Point, on the northwest shore of the lake, is an accumulation of almost flatlying tephra resulting from a sublacustrine pyroclastic eruption (Christensen and Gilbert, 1964) during the high-stand of Mono Lake (= Tioga time?).

The Mono Crater rhyolite obsidian and pumice complex south of the lake extends southward in a broad arc, convex to the east. The Inyo Craters continue this volcanic lineament farther south. The main complex of the Mono Craters represents considerably more than 50 volcanic events, perhaps separated by only short intervals of time. Recent potassium-argon age determinations by Dalrymple (1967) suggest ages of 5,000-6,000 B.P. for much of the complex. The lack of lakeshore features on most landforms of the main complex also indicate a post-Tioga age for this multiple volcanic event. A possible exception is an older andesite crater remnant near the northwestern end of the chain which may have a wavecut bench on its western face. The pattern of evolution of individual volcanos within the complex is recognizable. Pyroclastic eruptions of rhyolitic pumice from a central crater formed tephra rings, ramparts and cones, in most cases followed by emergence of tholiods or endogenous domes as, for example, at North (Panum) Crater where the tephra ring is still intact[4] Elsewhere, as at North and South Coulees, the viscous rhyolite-obsidian flows overran the tephra rim obliterating most of the initial-stage tephra features. In the northernmost rhyolite-obsidian coulee and possibly elsewhere, a

viscous second-stage tholoid emerged and expanded as a flow above the lower stage flow. Partially emergent tholoids, blowout craters and rhyolite-block pyroclastic craters are also identifiable. At a late volcanic stage, very recent pyroclastic eruptions covered much of the volcanic complex and surrounding lacustrine plain with ashfall tephra.

Lunar Analogues

Features of the area which might be regarded as analogous to certain features of the lunar surface include the subcircular volcanotectonic depression of Mono basin itself, small blowout craters throughout the area, circular tephra rims, and pumice plains of ashfall tephra. No proved examples of impact features are present.

GEOLOGIC FACTORS AFFECTING INFRARED IMAGE TONAL DENSITY

Radiative heat transfer

To analyze the geologic factors affecting image tonal density for the Mono area (Plates 2-6 and Figures 2-13) on July 27-28, 1966, we note that image tonal density obtained in the 8-14μ wavelength region is related to electromagnetic emission from the terrestrial surface in such a way that image tonal density as measured by a recording isodensitometer is a nonlinear function of blackbody-equivalent temperature of the surface (Figures 19-20; Table 2) as modified by instrumental and photographic processing factors.

Infrared image tonal density, thus, is largely controlled by those factors affecting its surface temperature. Stated theoretically, (I_N) is the intensity of radiation emitted by one cm^2 of a natural surface within a

specific wavelength range, per second, at temperature T. The following discussion demonstrates the role of emissivity (ε) of the natural surface in affecting I_N.

Radiation emitted in all directions by a blackbody within the wavelength interval $\lambda_1 - \lambda_2$, on the basis of Planck's law is given by

$$I_{BB} = \int_{\lambda'}^{\lambda^2} B(\lambda, T)\, d\lambda \qquad (1)$$

where $B(\lambda, T)$ is the amount of energy radiated from one cm^2 of a "black" surface at temperature T per second and per unit wavelength interval.

Radiance, N, from a natural surface is modified by the spectral emissivity, $\varepsilon(\lambda)$, according to:

$$I_N = \int_{\lambda'}^{\lambda^2} N(\lambda, T)\, d\lambda = \int_{\lambda'}^{\lambda^2} \varepsilon(\lambda)\, B(\lambda, T)\, d\lambda \qquad (2)$$

If $\varepsilon(\lambda)$ is known in the wavelength interval λ_1 to λ_2, I_N may be calculated from Equation (2). Alternatively, I_N and I_{BB} may be measured directly in the laboratory. Their relationship is then given in terms of the integrated bandpass emissivity, ε , as:

$$I_N = I_{BB} = \varepsilon \int_{\lambda'}^{\lambda^2} B(\lambda, T)\, d\lambda \qquad (3)$$

or the relationship between spectral emissivity ϵ_λ (emittance in Daniels, 1966) in the 8-14μ wavelength region and integrated bandpass emissivity ϵ may be as stated as

$$\epsilon = \frac{I_N}{I_{BB}} = \frac{\int_{8\mu}^{14\mu} \epsilon(\lambda) B(\lambda, T)\, d\lambda}{\int_{8\mu}^{14\mu} B(\lambda, T)\, d\lambda}$$

The ratio $\frac{I_N}{I_{BB}}$ or ϵ, integrated bandpass emissivity, for the 8-14μ wavelength region, has been determined in the laboratory for representative lithologies of the Mono area by Daniels (Table 3) using a Kern-Buettner-type emissivity box and Barnes IT-3 infrared thermometer. The results are reported in average digital values for the entire 8-14μ band. Spectral emissivity (emittance), ϵ_λ, for the 8-14μ band was determined in the laboratory by Daniels (1966) by comparison of continuous analog traces of the sample surface in contrast to a laboratory black body reference by means of a Black model I-4T Spectrometer (interferometer type). Results are reported in continuous analog curves giving emissivity variations over narrower spectral bands within the 8-14μ wavelength region than is possible with the Kern-Buettner emissivity box method of determining ϵ.

Certain generalizations can be made from the results of these laboratory emissivity studies.

The emittance spectra of acidic igneous rocks of the Mono area (rhyolite obsidian and pumice, rhyolitic ignimbrite of the Bishop tuff and quartz monzonite) are very similar and are spectrometrically difficult to distinguish from one another.[1] Their spectra, however, do differ from the

spectra of basalt. The spectra of weathered surfaces in general are still recognizable as the spectra of the underlying rock. The integrated emissivity (ε) determinations lead to a similar conclusion, that the averaged emissivity over the 8-14μ wavelength region is between 0.868 and 0.969 for these same rock types (Table 3). The effect of topographic irregularities in enhancing the apparent emissivity beyond even these values and in causing apparent emissivity differences greater than 0.1 (Figure 26) is discussed in a later paragraph of this report.

Wide differences in infrared emission from different materials were, however, recorded by the Reconofax IV scanner, suggesting that differences in surface temperature (Figures 19 and 20) are of considerable importance in affecting total emission and consequently image tonal density (Table 2).

The following discussion demonstrates the significance of thermal properties (β) of rock and soil materials, total reflectivity of the surface (r_o) and the diurnal maximum radiant flux, J_o, in controlling temperature of the earth's surface.

The temperature of a specific point on the terrestrial surface varies in a periodic way with the diurnal cycle. The dependence of the diurnal variation upon properties of the terrestrial surface has been calculated by Jaeger and Johnson (1953) using a simplified model for the thermal flux across the surface. The result is given by:

$$\theta_0 = \frac{F_0}{\beta}\left[\frac{\cos\lambda\cos\delta}{\omega^{1/2}}\sum_{n=1}^{\infty}\frac{2(\sin nh\cosh - n\cos nh\sin h)}{\pi n^{3/2}(n^2-1)}\cos\left(n\omega t - \frac{\pi}{4}\right)\right] \quad (4)$$

$$= \frac{F_0}{\beta} f(L, \delta, \omega, t)$$

Where Ts = Surface temperature

Fo = The net radiant solar flux across the solid terrestrial surface, i.e., the diurnal maximum radiant flux, J_o, incident upon the surface minus the reflected radiant flux, R_o.

β = Thermal inertia.

cos h = $-\tan\lambda \tan\delta$

ω = Angular velocity of the earth, 7.27×10^{-5} radians sec^{-1}.

δ = Solar declination

$\begin{cases} 19.3^\circ & \text{for July 27-28, 1966.} \\ 23.5^\circ & \text{for summer solstice.} \\ 0.0^\circ & \text{for autumnal equinox.} \end{cases}$

L = Latitude (38°N).

The function $f(L, \delta, \omega, t)$ is graphed for the summer solstice, the autumnal equinox and for July 27-28, 1966, for the latitude (38°N) of Paoha Island (Figure 21).

In order to compare these theoretical warming and cooling curves with surface temperature records, a mean daily surface temperature for a given point must be introduced into the theoretical curves such that:

$$Ts = Tmd + \frac{Fo}{\beta} f(L, \delta, \omega, t) \qquad (5)$$

where Tmd = mean daily surface temperature at a specific point. For the purpose of experimental comparison of theoretical diurnal temperature curves with recorded curves, the mean daily surface temperatures for two lithologies, lacustrine marl (Qm) and basalt lapilli-ash beach deposits

(QVb) at Black Point, have been assumed to be equal. A similar assumption has been made for two lithologies at Aeolian Buttes, Bishop Tuff (Qbt) and quartz monzonite (Ka).

Fo in Equation (4) is a measure of the peak thermal flux into the solid terrestrial surface. In terms of the peak radiant flux incident upon the surface, J_o, and the amount of this which is reflected, r_o, we have:

$$Fo = J_o (1-r_o) \qquad (6)$$

J_o is given for the south beach of Mono Lake for July 27-28, (upper curve, Epply pyrheliometer records, Figure 14). Total reflectivity, r_o, is dependent upon lithology and other factors and has been estimated from published absorption coefficients of solar radiation of various terrestrial materials and from recorded surface temperature curves (Table 4). In terms of J_o and the estimated reflectivity, r_o, the theoretical expression (4) for the diurnal temperature variations becomes:

$$To = \frac{J_o (1-r_o)}{\beta} f(L, \delta, \omega, t) \qquad (6b)$$

In actuality, the recorded temperature curves for two lithologies at Black Point and two lithologies at Aeolian Buttes resemble the theoretical curves and have the expected differences in amplitude (Figures 22-25). The theoretical curves were constructed using the best estimates and determinations for J_o, r_o (hence F_o) and β .

The recorded diurnal curves thus reasonably confirm that the F_o/β ratio does indeed control amplitude (Table 4) of the Black Point and Aeolian Buttes surface-temperature curves. Comparison of the Black Point and Aeolian Buttes theoretical curves with recorded temperature curves also significantly

confirms the role of r_o in estimating F_o and J_o.

The mean daily surface temperatures, Tmd, in Equation (5) have been assumed the same for the pairs of lithologies in the construction of Figures 23 and 25. Where r_o varies considerably, however, as at Black Point, this assumption yields theoretical curves which are too closely spaced in comparison to the recorded curves.

The recorded curve suggests a significantly lower mean daily surface temperature for marl (Qm) than for basalt lapilli-ash beach deposits (Qvb). This distinct surface temperature difference between Qm and Qvb throughout much of the diurnal cycle gives rise to one of the most outstanding features of the imagery (Plate 2) and isodensitracer scans (Figure 2-7) derived from the imagery of Black Point, i.e., the contrast between lacustrine carbonates and basalt pyroclastics.

A second point of difference is that the recorded surface temperatures between 10 p.m. and 7 a.m. (Qm, Qvb, Ka, and QbT) are higher than would be expected from the theoretical curves (Figures 22 and 24). An explanation of this disparity lies in the boundary condition at the surface leading to Equation (4) and (6b). The loss of heat from the surface is assumed constant throughout the day in this calculation. A more realistic assumption is that the loss of heat from the surface is dependent upon temperature. As the temperature decreases during the night, the loss would also decrease, yielding a lowered nightime cooling rate in accord with the recorded temperature curves.

The denominator, β in the F_o/β ratio, the thermal inertia characteristic of specific lithologies, is given by the following equation:

$$\beta = \sqrt{k \rho c} \qquad (7)$$

where k = thermal conductivity in cal cm^{-1} c^{o-1} sec^{-1}

ρ = bulk density in gm cm^{-3}

c = specific heat in cal gm^{-1} c^{o-1}

$$k = \kappa c \rho \qquad (8)$$

where κ = thermal diffusivity in cm^2 sec^{-1}

β is a measure of the rate of heat transfer at the interface between two dissimilar media. Literature data and U. S. Geological Survey laboratory determinations by Greene of thermal parameters of several lithologies sampled and imaged in the Mono area are given in Table 4. A direct logarithmic relationship between k and ρ for certain rock types (e.g., basalt) has been suggested by Robertson and Greene (Monthly Progress Reports, Branch of Theoretical Geophysics, U. S. Geol. Survey, December 1965 and December 1966).

From the foregoing, it is suggested that low bulk densities and/or low total reflectivity yield high F_o/β ratios and high amplitude surface temperature curves. If infrared image tonal density is a function of blackbody-equivalent temperatures of the surface as suggested by analysis of isodensitracer scans of the Mono imagery (Figures 2-13, 19 and Table 2), we may conclude that lithologies of low bulk density and/or low total reflectivity will be registered on infrared imagery in contrast to lithologies of high bulk density and/or high total reflectivity if all other factors are

equal. The contrast between lacustrine carbonates (Qm) and basalt pyroclastics (Qvb) of Black Point and Paoha Island represent wide differences in total reflectivity (Table 4).

Moreover, differential solar heating of the terrestrial surface during daylight hours occurs across uneven topographic surfaces because J_o, the incident radiant flux on the surface is dependent upon the inclination of the solar rays to the topographic surface. Such variations in J_o influence emission in the 8-14μ interval particularly during daylight hours, but also continue to affect 8-14μ range emission to a lesser extent at night (plate 5e and f) producing thermographic imagery of topography and microrelief. An extreme case occurs where thermal shadows in early morning and late afternoon imagery enhance surface textures (Plates 2a, 3a, 4a, 5a, 6a and b).

One additional type of radiative heat transfer to the atmosphere, dependent on topography, affected image tonal density during the July 27-28 survey period in the Mono area. Apparent emissivity (ϵ_c) which is dependent on surface roughness is more effective in influencing emission than is (ϵ) simply as a function of rock type (Table 3). This is demonstrated by graphs of change in apparent emissivity (ϵ_c) as a function of cavity shape (Figure 26). A surface composed of rock of uniform emissivity (ϵ) may exhibit variations in apparent emissivity, (ϵ_c), due to topographic relief. Figure 26 shows the dependence of upon the dimensions of a cylindrical cavity forming a depression in a surface of emissivity ϵ (Gouffé). Examples of situations intermediate between the latter two effects are common.

Radiative heat loss from the terrestrial surface in the Mono area during the period July 27-28, 1966, was affected by the interrelationship of four parameters characteristic of specific lithologies, a fifth dependent on topography and microrelief and a sixth on surface texture:

1) thermal diffusivity (α)
2) specific heat (C)
3) bulk density (ρ)
4) total reflectivity (r_o)
5) total radiant energy incident on the surface (J_o) as a function of topography.
6) apparent emissivity (ε_c) as a function of surface roughness and blackbody cone effects.

Convective heat transfer

Convective heat loss from fractures heated by the movement of epithermal solutions or gases, detected on night and pre-dawn imagery, provides a means for outlining the surface configuration and estimating the intensity of thermal anomalies associated with hot springs and fumaroles at Paoha Island (Plate 3a, d, e, and f) and Deschambeau Ranch at Black Point (Plate 2a, d, e, and f).

Hot spring activity in the Mono Basin and specifically on Paoha Island has long been known and was first reported by Russell in 1889; the present status, distribution and structural control of hot springs and fumaroles here continues to be a subject of interest. A decline in the level of Mono Lake since 1955 made possible the detection of an array of distinct points of convective heat loss ringing the southeastern peninsula of the island

where remnants of a recent andesite-basalt volcano are exposed through a carapace of lacustrine deposits (Figure 27 and Plate 7a and b).

Surface temperature at the apertures of hot springs ranged up to 85°C at several points based on measurement with a bimetallic thermometer on July 25, 1966. This thermal activity bears a superficial resemblance to that of several other active volcanic areas including the classic andesite caldera of Santorin (Thíra) volcano in the Cyclades archipelago (Figure 28). Santorin is now known to have had two Krakatoan eruptions 25,000 and 1400 B.C. More than 1000 years after the second, Néa Kaïmeni, the Santorin analogue of Paoha, emerged as a central island crater in the subsided caldera. Since then, recurrent volcanic activity has occurred in the area of Néa Kaïmeni. Recent Russian reports (Butuzova, 1966) indicate continued hot spring and fumarolic activity around the periphery of Néa Kaïmeni.

Other possibly analogous volcanotectonic depressions in the Philippines and Indonesia have similar morphology and distribution of thermal points around a resurgent central crater island which has been the locus of the most recent activity. The analogy should not be pressed too far, yet if we consider the evidence of differential uplift involving deformation of the carapace of lacustrine deposits of Paoha (plate 7c), the gravity low centered on the island (Pakiser, 1964), the volcanic morphology (Plate 7d) of Paoha (as well as of its neighbor, Negit) and the greatest concentration of thermal points in Mono caldera around Paoha, it seems likely that the Paoha-Negit Islands area was indeed the most recent locus of volcanism in Mono basin, that the fumaroles and hot springs may represent late-volcanic

activity and that Mono caldera as suggested by Pakiser and others (1960) should indeed be regarded as one of the areas of active albeit late-stage volcanism in the United States.

Other anomalies

Two additional types of anomalies were noted on imagery of the Mono area: the first associated with thermal currents in the Mono Lake where hot springs discharge into effluent ponds at Black Point (Plate 2a, d, e and f) and into Mono Lake from points along the north shore and peripheral to Paoha Island. (Plate 3a, d, e and f). Secondly, negative daytime anomalies in saturated unconsolidated materials, e.g., a playa surface on Paoha Island (Plate 3d), suggest that evaporation and lateral heat transfer change in specific small areas where a thermal near-equilibrium has been established.

SUMMARY

Field and laboratory studies of infrared imagery of the terrestrial surface of the Mono Lake area, California, during July 27-28, 1966, conform that interplay between several physical and thermal parameters of surface materials controls radiant emission from the surface in the 8-14μ wavelength interval. The following physical properties and processes in addition to meteorologic factors probably have the greatest influence:

A) Emissivity of the surface as a function of surface roughness, topographic blackbody cone effects and to a considerably lesser extent, as a function of lithology.

B) Radiative heat loss dependent on the following properties of the surface.

1) thermal diffusivity (α)
2) specific heat (C)
3) bulk density (ρ)
4) total absorptivity, ($1-r_o$), integrated over the entire solar spectrum
5) radiant flux intensity (J_o) as a function of inclination of solar rays to the topographic surface

C) Convective heat loss from,

1) structures heated by circulating epithermal solutions
2) actual surface discharge of hot springs and fumaroles representing late-volcanic activity mostly on or near Paoha Island.
3) thermal currents in Mono Lake associated with cold and hot spring discharge.

D) Evaporative cooling and lateral heat transfer by conductive and convective mechanisms in saturated unconsolidated materials and by air movement or entrapment in and around talus slopes and surfaces having complicated microrelief.

To determine the relative importance of these physical properties and heat transfer processes, ground surface-temperature and radiant flux intensity monitoring were found to be useful as were meteorologic records. Field measurement of thermal parameters and total solar reflectivity should also be carried out in future surveys preferably as part of the ground

monitoring procedures simultaneously with infrared imaging overflights. A sequence of overflights during the 24-hour diurnal cycle at Mono Lake provided data for diurnal surface temperature curves. Construction of theoretical warming and cooling curves for the same surface materials permitted comparison with observations and estimation of either the thermal inertia (β) or total reflectivity (r_o) where other parameters plus the radiant flux intensity (J_o) were known.

Comparison of recorded temperature curves with theoretical curves confirmed that the F_o/β ratio does indeed control amplitude of the surface temperature curves and that this ratio is a function of the parameter $(1-r_o)$, a characteristic property of specific lithologies. Comparison of $\overline{\beta}$ image tonal densities by means of an isodensitometer scanning technique indicate that variations in amplitude (or variations in time-rate of change) of diurnal temperature curves are detectable by means of infrared imagery provided radiant flux intensity is known, that meteorologic and hydrologic factors do not interfere and that topography and microrelief are simple. Where topography, vegetation, saturation and meteorologic factors do not affect the F_o/β ratios, many rock types having characteristic F_o/β ratios are distinguishable though not categorically identifiable. Because β generally increases with bulk density and F_o is related to absorptivity $(1-r_o)$, so that $T_o \sim f\left[J_o \quad \frac{(1-r_o)}{\beta}\right]$ lithologies of high density and/or high albedo contrast sharply with lithologies of low density and/or low albedo. Thus, with sufficient ground monitoring data to support infrared imagery surveys the geologic contacts, if exposed, between bedrock and

unconsolidated materials, between volcanic flows and low-density pyroclastics, between iron-rich volcanic rocks and light-colored carbonates and similar contrasting lithologies can be distinguished.

The best time of day in California in July and August for detection of thermal anomalies involving convective heat loss, is 8:00 p.m. - 6:00 a.m. Maximum distinctions between surface materials, arising from differences in the F_o/β ratio occur between 3:00 and 7:30 p.m., but thermographic effects from the surface mask these distinctions. The thermographic effects diminish after sunset faster than the decline in emission related to the F_o/β ratio as a property of materials. 8:00 - 10:00 p.m. is thus a good period for maximum distinction of lithologies, but a sequence of surveys from 8:00 p.m. to 4:00 a.m. showing different rates of cooling is best for delineating lithologic units.

FOOTNOTES

/1 Petrographic studies by Kenneth LaJoie, University of California, Berkeley, reported since completion of this paper, indicate that the volcanics of Paoha and Negit Islands are of rhyodacitic composition.

/2 Recent work by R.J.P. Lyon, Stanford University suggests that careful computer programming of the infrared emittance spectra of acidic igneous rocks of the Mono area permits identification of several more rock types.

/3 See p. 5.

/4 Recent absolute age dating by Irving Friedman, U.S.G.S. suggests an age of less than 2,000 years for this endogenous dome.

/5 Reported by LaJoie to be highly diatomaceous.

Explanatory Material to Accompany Plate I

Geologic Map of the Mono Craters Area, California

EXPLANATION

GEOLOGIC AGE	DESCRIPTION	
	Sedimentary Rocks	Igneous Rocks
Recent	Qb - Beach deposits of Mono Lake including calcareous lacustrine deposits (Qm) and deltaic deposits (Qal).	
Recent	Qt - Sliderock of talus and coulee front. Qf - Fan and slopewash deposits Qal - Stream and other alluvial deposits including reworked ashfall deposits. Qlt - Dissected stream-cut terraces in lacustrine deposits with some Qal.	
Recent	Qm - Lacustrine marl and diatomite of Paoha Island	QpvA - Andesite and andesitic basalt flows of Negit and Paoha Islands; associated fumarolic activity. QpA - Pumice tephra (ash and lapilli) - A) ashfall veneer and barren pumice sandflats. QpB - B) same with vegetation and minor relief.

GEOLOGIC AGE	DESCRIPTION	
	Sedimentary Rocks	Igneous Rocks
Recent		Qyrc - Younger pumiceous rhyolite obsidian of coulees. Qyrt - Younger rhyolite and obsidian of volcanic domes in places with overlying Qyrp. Qyrb - Younger obsidian and rhyolite of block craters. Qyrp - Younger tephra (lapilli, ash) rings, ramparts and cones/
	Ql_1 - Lacustrine deposits, including older deltaic gravels; includes overlying Qyrp east and southeast of North Crater.	Qvb - Reworked basalt lapilli-ash beach deposits of Black Point.
Pleistocene	Qti - Till and moraines of the Tioga Glaciation; some deltaic gravels	Qbpb - Olivine basalt lapilli-ash pyroclastic deposits of Black Point. Qor - Older rhyolite domes and flows. Qam - Andesite of Mono Craters. Qjlb - Basalt of June Lake Junction.
	Qta - Till and moraines of the Tahoe Glaciation	
Pleistocene		Qbt - Bishop Tuff - rhyolite ignimbrite

GEOLOGIC AGE	DESCRIPTION	
	Sedimentary Rocks	Igneous Rocks
Pleistocene		
Cretaceous		Ka - Quartz monzonite of Aeolian Buttes.
Cretaceous and older	Ms - Metasedimentary and other crystalline rocks.	ms - Metasedimentary and other crystalline rocks

Flow ridges on coulee surfaces, trend generally transverse to direction of movement.

Explosion craters or vents in pyroclastic deposits, rhyolite or andesite-basalt extrusives.

Contacts

Inferred faults

Note of age relations within the main crater complex and at Black Point

Potassium-argon absolute-age determinations (Dalrymple, G. B., informal communication, 1966) indicates most of the main crater complex is Recent in age, i.e., post-Tioga glaciation.

Cutting relations indicate Qyrc, Qyrt, Qyrb and Qyrp are younger than contiguous Qor units, but they are probably not contemporaneous in different parts of the map area. At least one Qyrc unit (South Coulee) is younger than Qta which it transects. Most of the rhyolite-obsidian units are also post-Tioga glaciation (post-Qti and in part post-Q_{l_1}), with possible exception of some Qor, based on the following evidence: Qyrc, Qyrt, Qyrb, Qyrp and some Qor appear to overlie Q_{l_1} and none of these units shows morphologic evidence of a Tioga-age Mono Lake shoreline. The crater complex actually overlies landforms on which the Tioga Mono Lake shoreline is cut in the vicinity of North Coulee. The generally south-trending bench on the west side of Qam (a dissected volcano, one of the oldest in the Mono complex) may be a vestige of the Tioga shoreline, suggesting that Qam is pre-Tioga. Similar shoreline features appear on unconsolidated materials overlying Qjbl one mile farther south.

Qbpb of Black Point may be the product of a sublacustrine eruption (Christiansen and Gilbert, 1964) suggesting that Qbpb accumulated during the Tioga highwater level of Mono Lake.

See map in back of this document.

(Plate 1)

Plate 2

Infrared imagery. 8-14μ wavelength region. July 27-28, 1966 Black Point, California. 2A) 0725 hours, 2B) 1157, 2C) 1631, 2D) 2029, 2E) 2359, 2F) 0400. Note reversal of image density of water and land areas during the diurnal cycle. Relative change in radiance of lithologic surfaces indicates different F_o ratios for $\overline{\beta}$ a) Qvb; b) Qm, c) Qal. Maximum lithologic distincitions are apparent between 2000 and 2400 hours. Convective heat loss from effluent ponds d) retaining discharge from thermal spring is most striking between 2000 and 0400. Maximum effect of differential solar heating of topographic surface appears here at 0725. Thermal currents in lake (e) are probably due to cold spring discharge. Area of isodensitracer scans shown by rectangles (f): approximately same areas were scanned for surveys a) - f). Ground monitoring station g), located near geologic contacts between Qvb, Qm and Qal, was instrumented with an automatic-recording multiple thermistor-probe variable sequencer system to establish diurnal surface temperature variation of several lithologies; a similar thermistor-probe telethermometer system was operated at h); Tempscribes, recording thermograph, and bulb thermometers were utilized to determine surface and thermal spring effluent temperatures at i).

0725

1157

1631

2029

2359

0400

Plate 3

Infrared imagery, 8-14μ wavelength region. Paoha Island, Mono Lake, California, July 27-28, 1966. 3A) 0811 hours 3B) 1207, 3C) 1612, 3D) 2010, 3E) 0007, 3F) 0407. Lithologic distinctions arising from the $\frac{F_o}{\beta}$ parameter are most definitive at 2010. Note that emission from (a) $Q_{pv}A$ is greater to the northwest where pyroclastics grade into a basaltic lava flow. Emission from thickest part of the lava flow remains highest through 0407 survey. (b) Northern part of Q_m, rich in ashfall components, shows greater emission than (c) southern three quarters of Q_m area. Lowest emission throughout diurnal cycle is from salt-pan evaporites in (d) pit of pyroclastic crater and in (e) blowout crater. On western side of island, (f) wet evaporating pan or playa surface exhibits high radiance from its center during nightime surveys but the darker color resembles dry evaporites in tonal density. Morning imagery (0811) shows best topographic detail: note (g) transecting pyroclastic craters, (h) lava flow ridges, (i) landslip topography, (j) wavecut bench and remnants of former shoreline. Thermal anomalies (k) representing convective heat loss from thermal springs and fumaroles and related thermal currents in the lake are distinct from 2010 through 0811 surveys. Cold currents (l) representing discharge from springs are most clearly delineated at 0811, but are partially visible (l') on nightime imagery. Area of isodensitracer scans shown by rectangles M; approximately same areas were scanned for surveys a) - f).

0811

1207

1612

2010

0007

0407

Plate 4

Infrared imagery of Aeolian Buttes, three miles west of Mono Craters complex, California. 8-14μ wavelength region. July 27-28, 1966: 4A) 0758 hours, 4B) 1204, 4C) 1603, 4D) 2029, 4E) 2359, 4F) 0400. Bedrock outcrops of Aeolian Buttes inlier exhibit lower-amplitude diurnal surface temperature change than surrounding unconsolidated material; note reversal in comparative image tonal density. (a) Innermost outcrops in Buttes area are quartz monzonite (Ka); (b) outer ring represents exposures of upper units of Bishop tuff (Q_{bt}); (c) unconsolidated materials are largely lucustrine deposits (Q_{l_1}) overlain by Recent tephra layer of pumiceous rhyolite lapilli and ash (Q_{yrp}). Slightly greater nightime emission from quartz monzonite (Ka) than from Bishop tuff (Q_{bt}) outcrops can be attributed to higher thermal inertia of quartz monzonite. Unconsolidated tephra layer (Q_{yrp}) has lower thermal inertia and higher total reflectivity than either type of bedrock. Ground monitoring station (d) located on geologic contact between quartz monzonite and upper units of Bishop tuff was instrumented with automatic-recording Barnes IT-2 and IT-2 fixed-field radiometers and meteorologic equipment during period of survey.

0758

1204

1603

2029

2359

0400

Plate 5

Infrared imagery. 8-14μ wavelength region. July 27-28, 1966 North coulee, Mono Craters rhyolite-obsidian complex. 7a) 0811 hours, 7b) 1207, 7c) 1641, 7d) 2038, 7e) 0033, 7f) 0407. Maximum topographic effect appears at 0811. Relative change in radiance during the diurnal cycle reflects different $\frac{F_o}{\beta}$ ratios for unconsolidated material and bedrock.

a) Qp, rhyolite pumice tephra (ash and lapilli). b) Q_{yrp}, rhyolite pumice tephra rings and cones, c) Q_{yrt}, rhyolite and obsidian of tholoids with overlying Q_{yrp} in places and d) Q_{am}, andesite. Upper stage of tholoid (c) shows relatively different radiance during the diurnal cycle than lower stage, suggesting that the upper stage is composed of blocky rhyolite and obsidian devoid of fine pyroclastics as is small subsidiary cone at e). Ashfall tephra coating much of lower stage may indicate pyroclastic eruptions from the volcanic complex immediately to the south between time of formation of lower and upper stages of North Coulee tholoid. Low nightime emission from troughs (f), between flow ridges of lower stage may be the result of interplay of several factors: concentrations in the troughs of fine pyroclastics having low thermal inertia, blackbody cone effect of troughs causing increased emissivity thus entailing greater heat loss at night, and topographic effect on incident solar radiation during the day causing thermal shadows and lower surface temperatues of walls of troughs. Movement of denser cool air in troughs may also contribute to lower temperatures in troughs.

0811

1207

1641

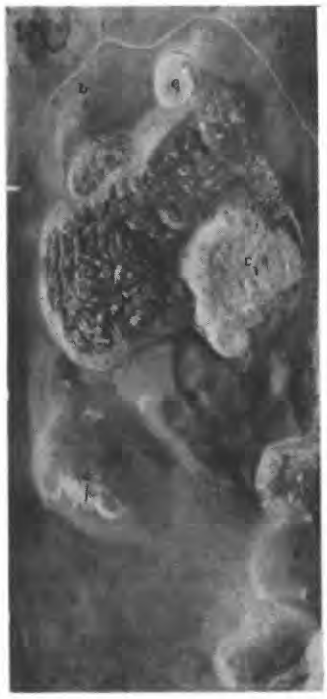

2038

0033

0407

Plate 6a and 6b

Infrared imagery of the main rhyolite-obsidian complex at Mono Craters. 8-14μ wavelength region. 0800, June 4, 1965. Major effect in early daytime imagery is the enhancement of topographic and microrelief features subject to the most direct solar heating. Intensity of the incident radiant flux is dependent upon the inclination of solar rays to the topographic surfaces; emission in the 8-14μ interval from the surface is a function of this insolation.

Thermal shadows are the result of relatively low emission from cooler shaded areas. These effects in early morning imagery accentuate textural patterns, microrelief, low-order relief features and other geomorphic details. Note: a) outlines and texture of slopewash and fan deposits west of crater complex; b) texture and lineaments in pumiceous tephra east of crater complex; c) details of crater morphology - particularly in dissected pyroclastic cones and explosion pits of main range; c_1) late-stage explosion pit in bedrock of Punchbowl; c_2) tholoid completely enclosed by older tephra ring, d) flow ridges and outflow centers in rhyolite-obsidian tholoids and coulees; d_1) vertical turreted tholoid of Wilson Butte, d_2) biscuit-shaped obsidian-rich Glass Mountain tholoid and flow with prominent flow ridges and outflow centers; e) outcrop pattern of June Lake basalt sheet west of crater complix; f) configuration of Tahoe-age morainic ridges near Aeolian Buttes and South Coulee; g) Aeolian Buttes inliers of quartz monzonite ringed by upper units of Bishop tuff; h) wet spot (dark) in center of pumiceous sand flat east of Punchbowl, suggestive of playa conditions.

7 AM?

Plate 6a

8 AM?

Plate 6b

presumably Taken at different times

Plate 7

7A Thermal spring and fumarolic deposits forming a southward-jutting peninsula along the probable extension of a fracture zone, eastern Paoha Island.

7B Recent andesite-basalt volcanics ($Q_{pv}A$) cut by fracture zones containing epithermal or thermal-spring deposits. Hot springs are concentrated along lakeward extension of fracture zones.

7C Structural deformation of lacustrine deposits (Q_m) of wavecut bench, western Paoha Island.

7D Northern Paoha and Negit Islands. View west. Note transecting pyroclastic craters in foreground and rough-surfaced flow forming ridge (a) in right middleground. Andesite-basalt crater and flows (b) of Negit Island appear in right background. Highly reflective diatomaceous lacustrine deposits (c) form a rim around volcanics of both Paoha and Negit Islands.

B

D

A

C

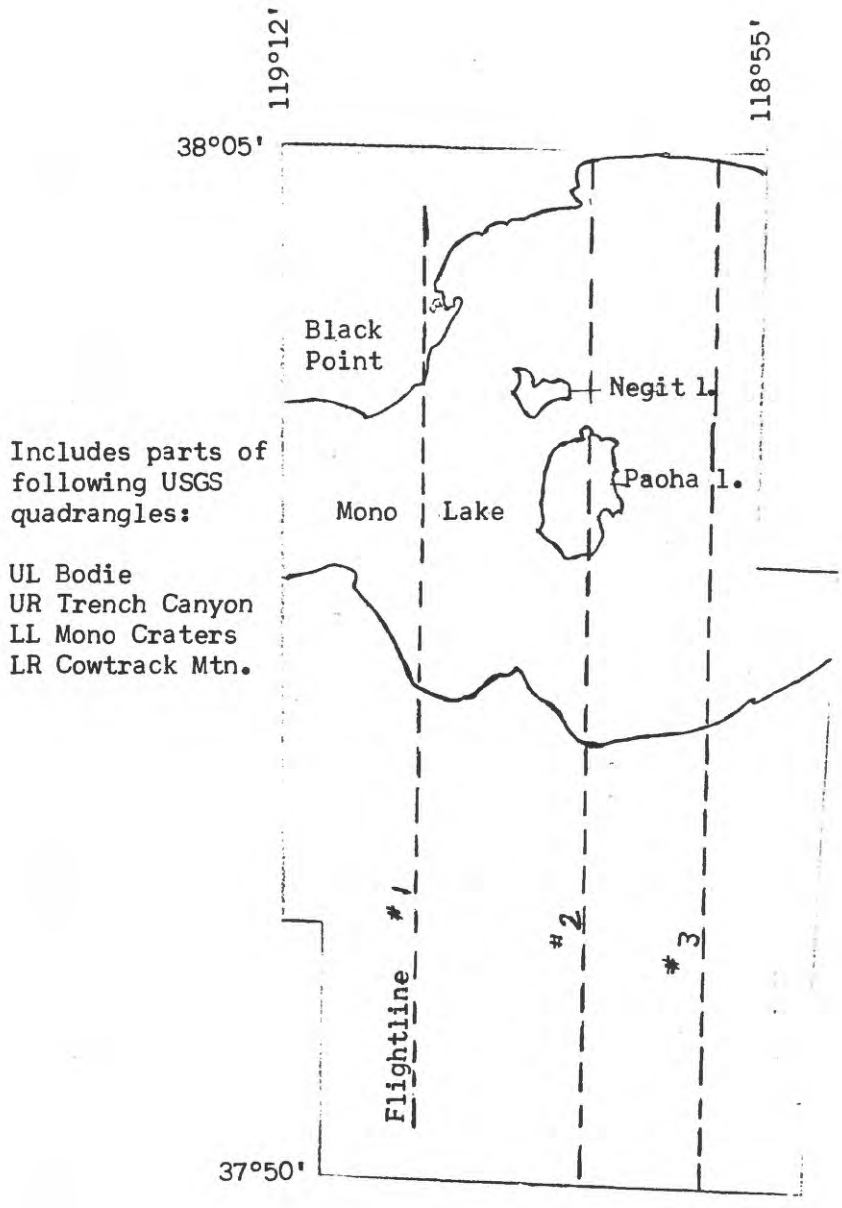

Scale: Approximately 1:190,000

Figure 1. Flightlines, infrared imagery surveys, July 27-28, 1966, Mono Craters area

Figure 2. Legend

Isodensity Scan of IR Imagery, Wilson Creek Delta

Black Point, Mono Lake 0750 7/27/66 Line 1

10X magnification

MAP UNIT			RELATIVE FILM DENSITY
	Color	Pattern	Hot
			.60
a	RED	Dash	.56
		Dot	.52
		Space	.48
b	BLUE	Dash	.44
		Dot	.40
		Space	.36
c	BROWN	Dash	.32
		Dot	.28
		Space	.24
d	GREEN	Dash	.20
		Dot	.16
		Space	.12
e	BLACK	Dash	.08
		Dot	.04
		Space	0.00
			Cold

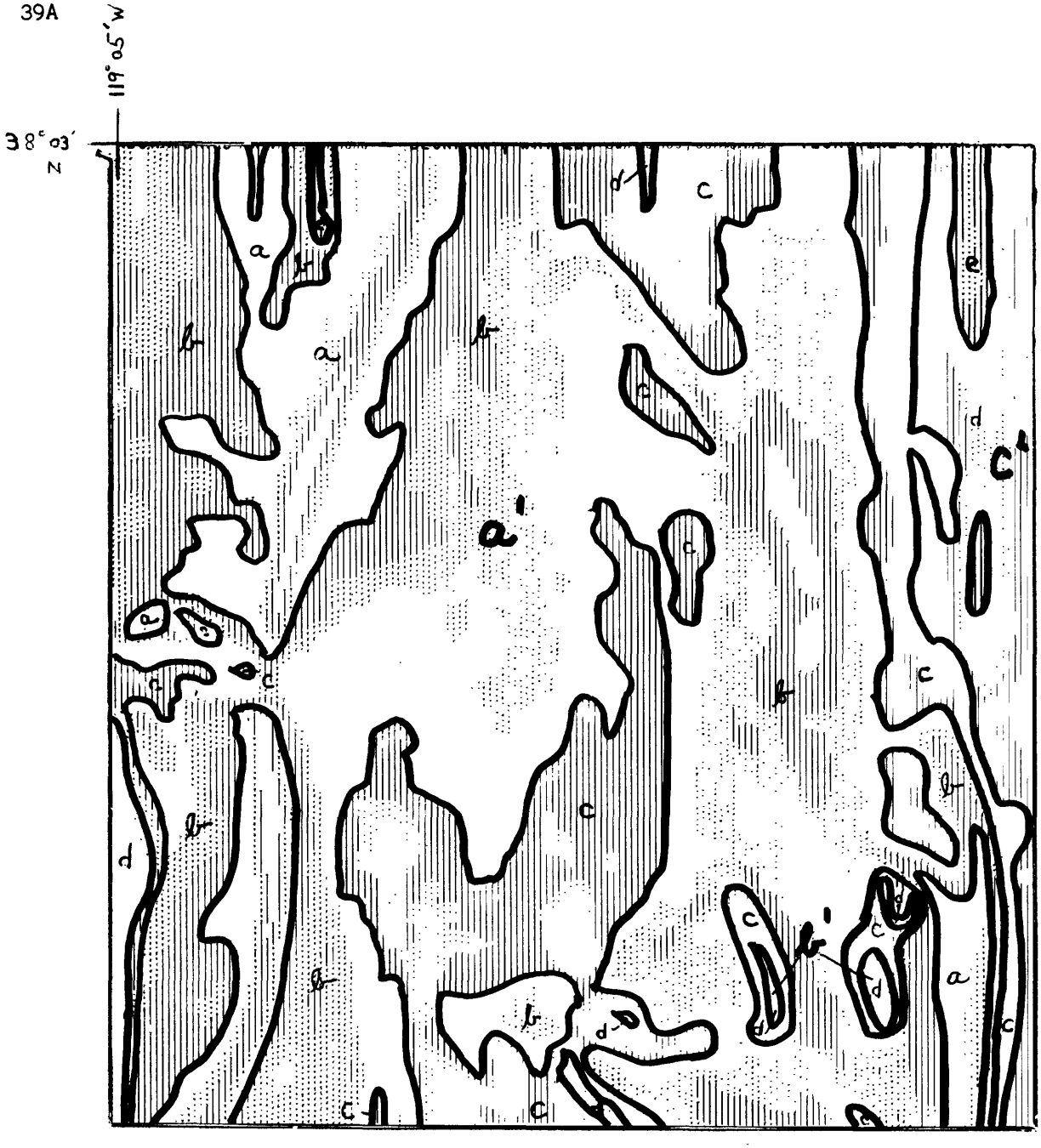

Figure 2. Isodensity scan used in correlating surface temperatures with image emulsion density scale (Figures 19 and 20).

a1) Generally silty surface (Qb) of Wilson Creek delta.
b1) Evaporating pans of lacustrine carbonates (Qb), and
c1) Mono Lake

Figure 3. Legend

Isodensity Scan of IR Imagery, Wilson Creek Delta, Black Point

Mono Lake 1233 7/27/66 Line 1

10X magnification

MAP UNIT			RELATIVE FILM DENSITY
	Color	Pattern	
a	RED	Dash	.96D
		Dot	.84
		Space	.72
b	BLUE	Dash	.60
		Dot	.48
		Space	.36
c	BROWN	Dash	.24
		Dot	.12
		Space	.00D

Hot ↑ ↓ Cold

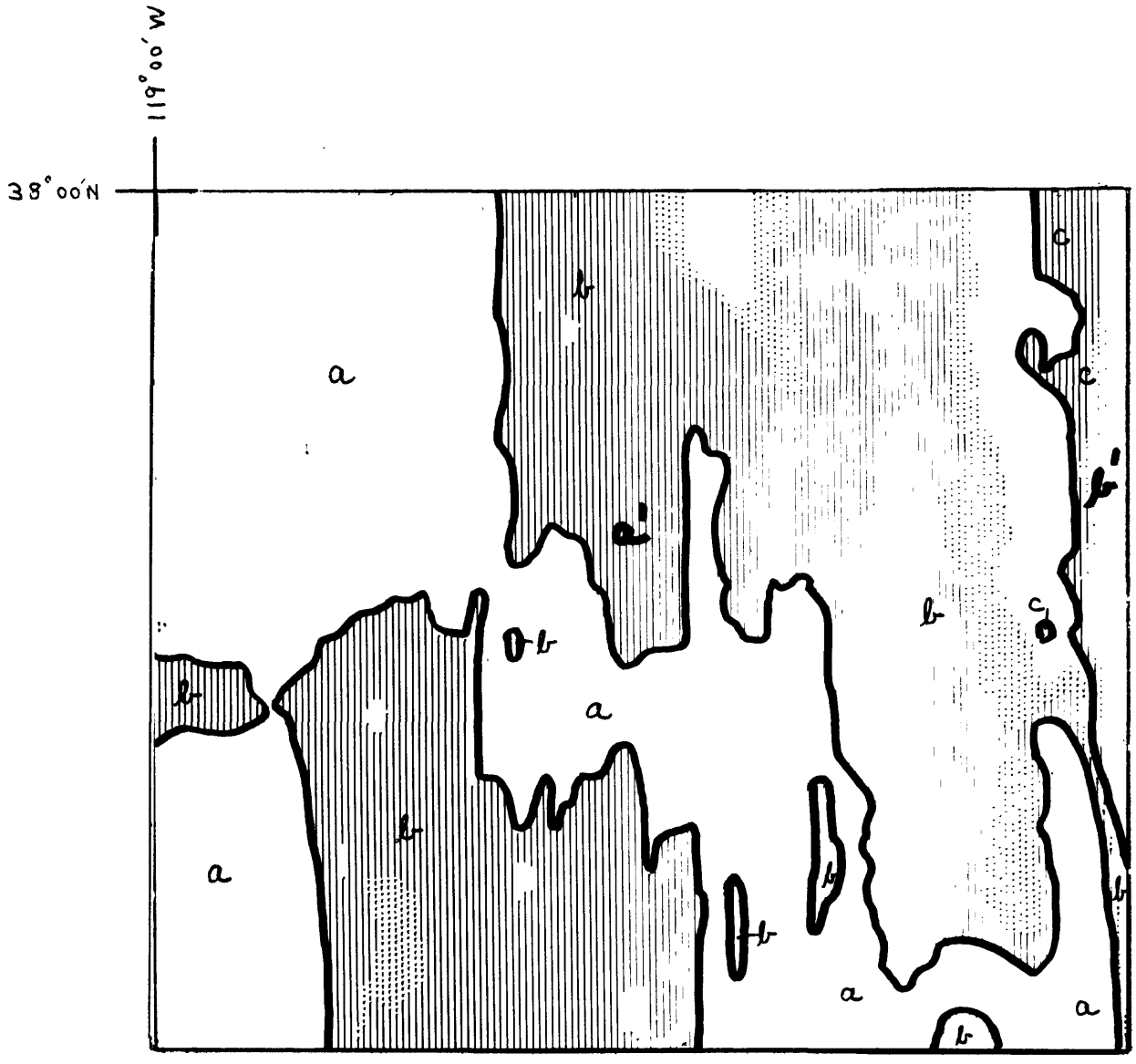

Figure 3. Isodensity scan used in correlating surface temperatures with image emulsion density scale (Figures 19 and 20).

a[1]) Lacustrine silt (Qb) of Wilson Creek delta.
b[1]) Mono Lake.

Figure 4. Legend

Isodensity Scan of IR Imagery of Wilson Creek Delta, Black Point

Mono Lake 1631 7/27/66 Line 1

10X magnification

MAP UNIT			RELATIVE FILM DENSITY
	Color	Pattern	Hot ↑
a	LAVENDER	Dash	.96
		Dot	.84
		Space	.72
b	RED	Dash	.60
		Dot	.48
		Space	.36
c	BLUE	Dash	.24
		Dot	.12
		Space	.00D
			↓ Cold

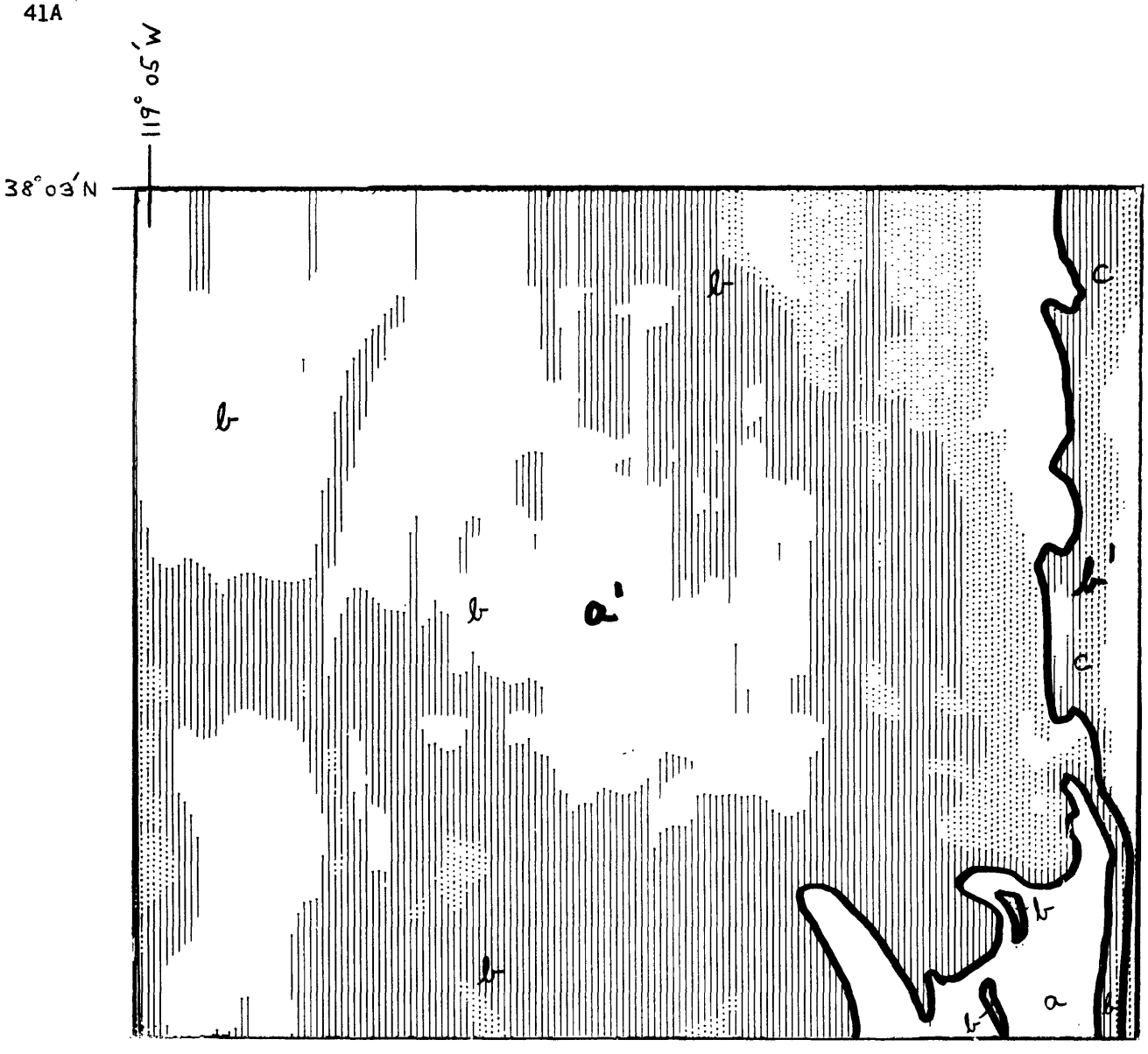

Figure 4. Isodensity scan used in correlating surface temperatures with image emulsion density scale (Figures 19 and 20).

a[1]) Lacustrine silt (Qb) of Wilson Creek delta.
b[1]) Mono Lake.

1/10 MILE
SCALE

Figure 5. Legend

Isodensity Scan of IR Imagery, Wilson Creek Delta, Black Point, Mono Lake 2008 7/27/66 Line 1

10X magnification

MAP UNIT			RELATIVE FILM DENSITY
	Color	Pattern	
a	RED	Dash	.96
		Dot	.84
		Space	.72
b	BLUE	Dash	.60
		Dot	.48
		Space	.36
c	BROWN	Dash	.24
		Dot	.12
		Space	.00

Hot

Cold

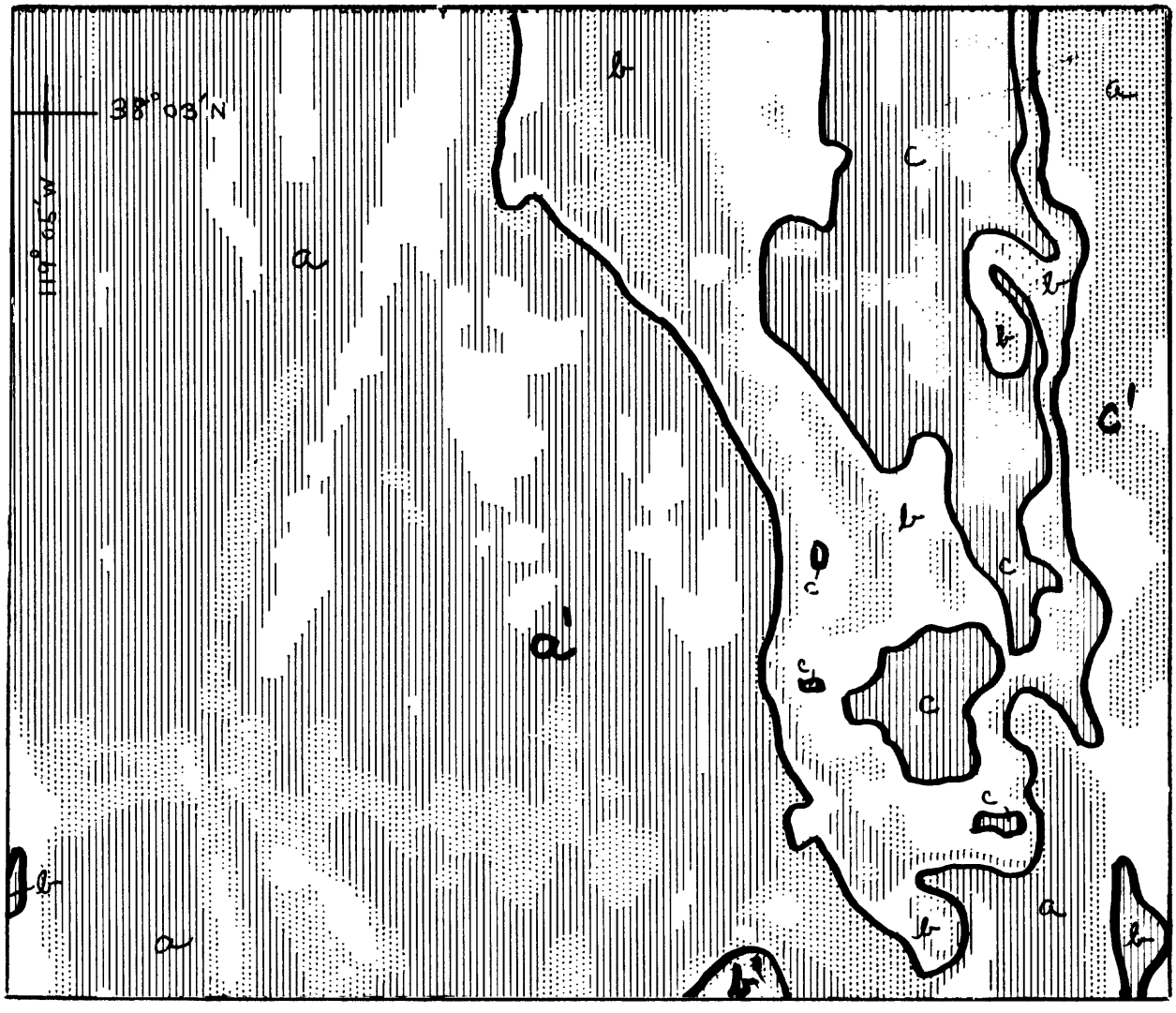

Figure 5. Isodensity scan used in correlation of surface temperatures with the image emulsion density scale (Figures 19 and 20).

a[1]) Lacustine silt (Qb) of Wilson Creek delta.
b[1]) Highly reflective evaporites (Qb) and
c[1]) Mono Lake.

Figure 6. Legend

Isodensity Scan of IR Imagery of Wilson Creek Delta, Black Point, Mono Lake 0404 7/28/66 Line 1

10X magnification

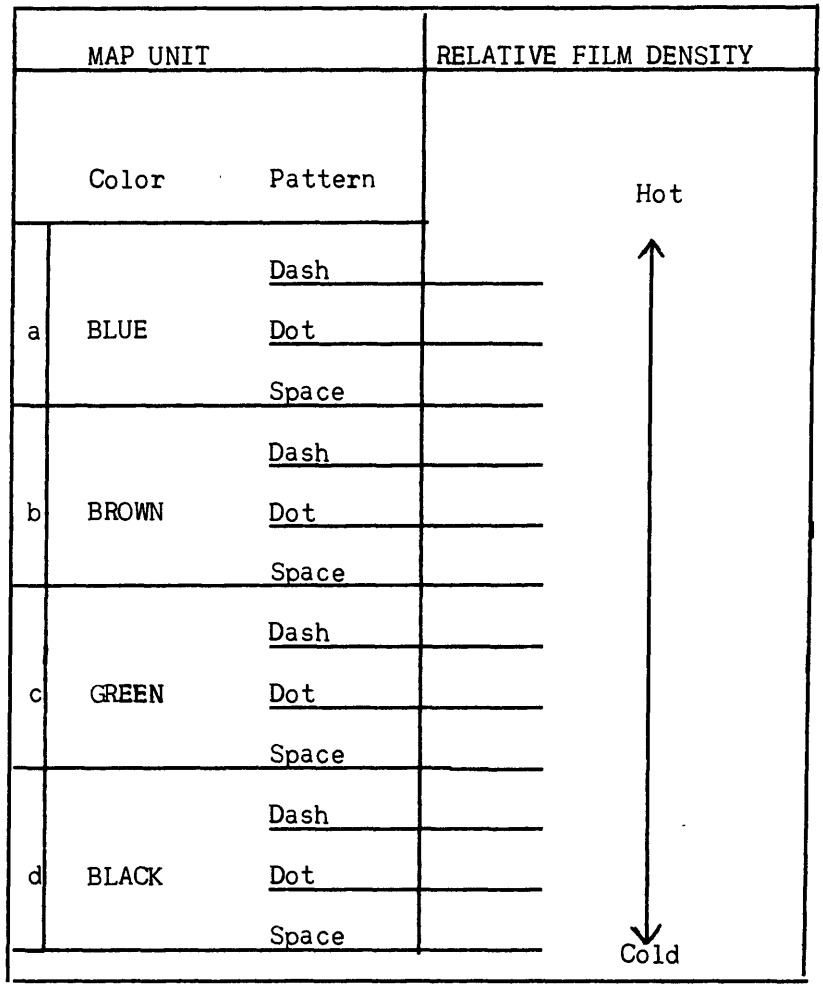

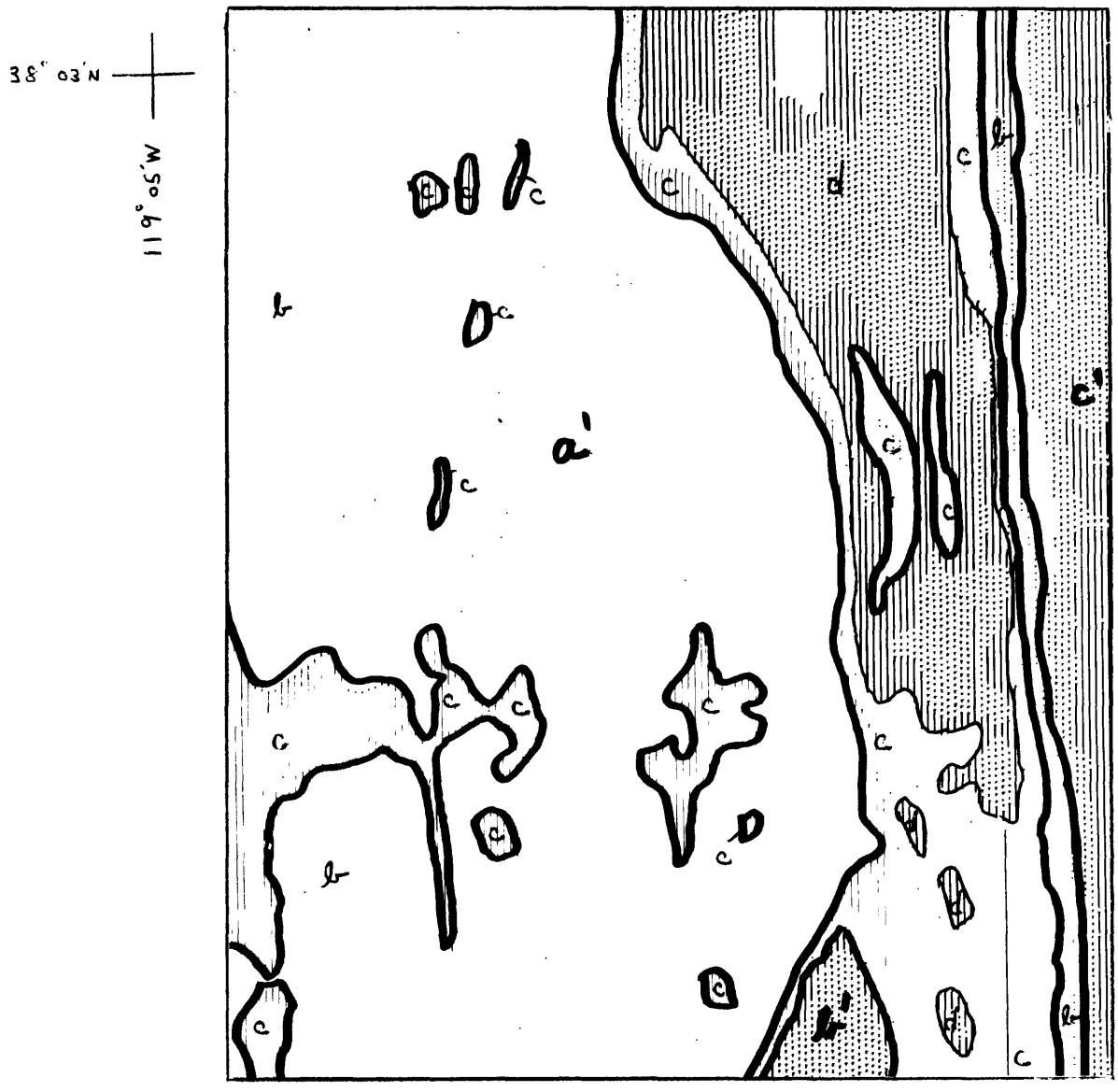

Figure 6. Isodensity scan used in correlating surface temperatures with the image emulsion density scale (Figures 19 and 20).

a[1]) Lacustrine silt (Qb) of Wilson Creek delta,
b[1]) Highly reflective evaporites (Qb) and
c[1]) Mono Lake

Figure 7. Legend

Isodensity Scan of IR Imagery of Wilson Creek Delta,

Black Point, Mono Lake 0404 7/28/66 Line 1

10X magnification

MAP UNIT		RELATIVE FILM DENSITY
	Pattern	Hot ↑
a	Dash	1.20
	Dot	1.00
	Space	.96
b	Dash	.84
	Dot	.72
	Space	.60
c	Dash	.48
	Dot	.36
	Space	.24
d	Dash	.12
	Dot	.00D
	Space	
		↓ Cold

Figure 7. Isodensity scan used in correlating surface temperatures and the image emulsion density scale (Figures 19 and 20).

a^1) Lacustrine silt (Qb) of Wilson Creek Delta
b^1) Highly reflective evaporites (Qb) and
c^1) Mono Lake

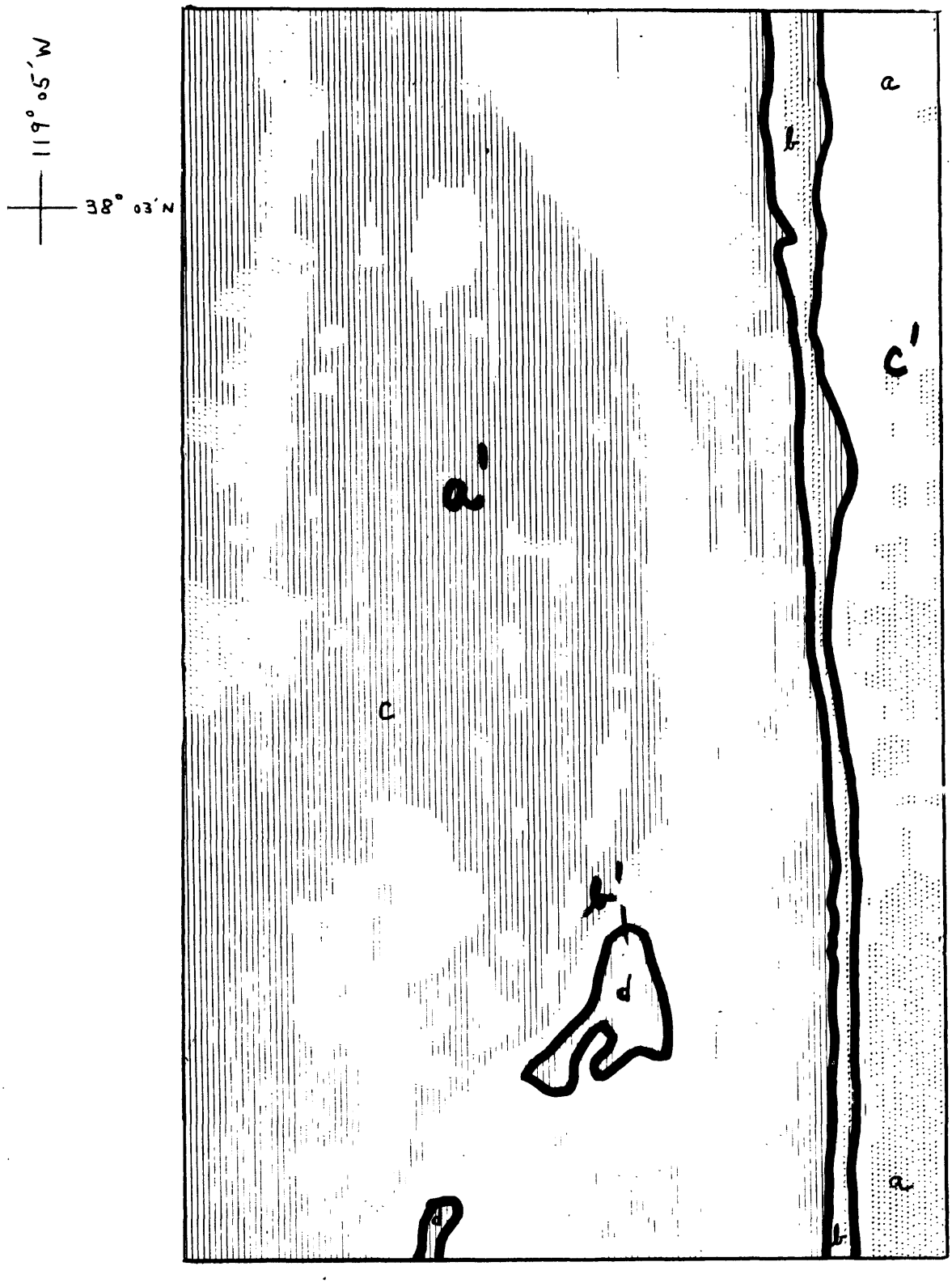

FIGURE 7

1/10 MILE
SCALE

Figure 8. Effluent from a hot spring near Deschambeau Ranch, Black Point. Ground temperature measurements confirm that the middle pond (a^1) is warmer than the southeasternmost pond. Note contrast in radiance between ponds and adjacent marshy vegetation at (b^1).

5A

ISODENSITY SCAN OF IR IMAGERY: DECHAMBEAU RANCH, BLACK POINT, CALIFORNIA

7/27/66 2359 HOURS LINE 1 10 X MAGNIFICATION

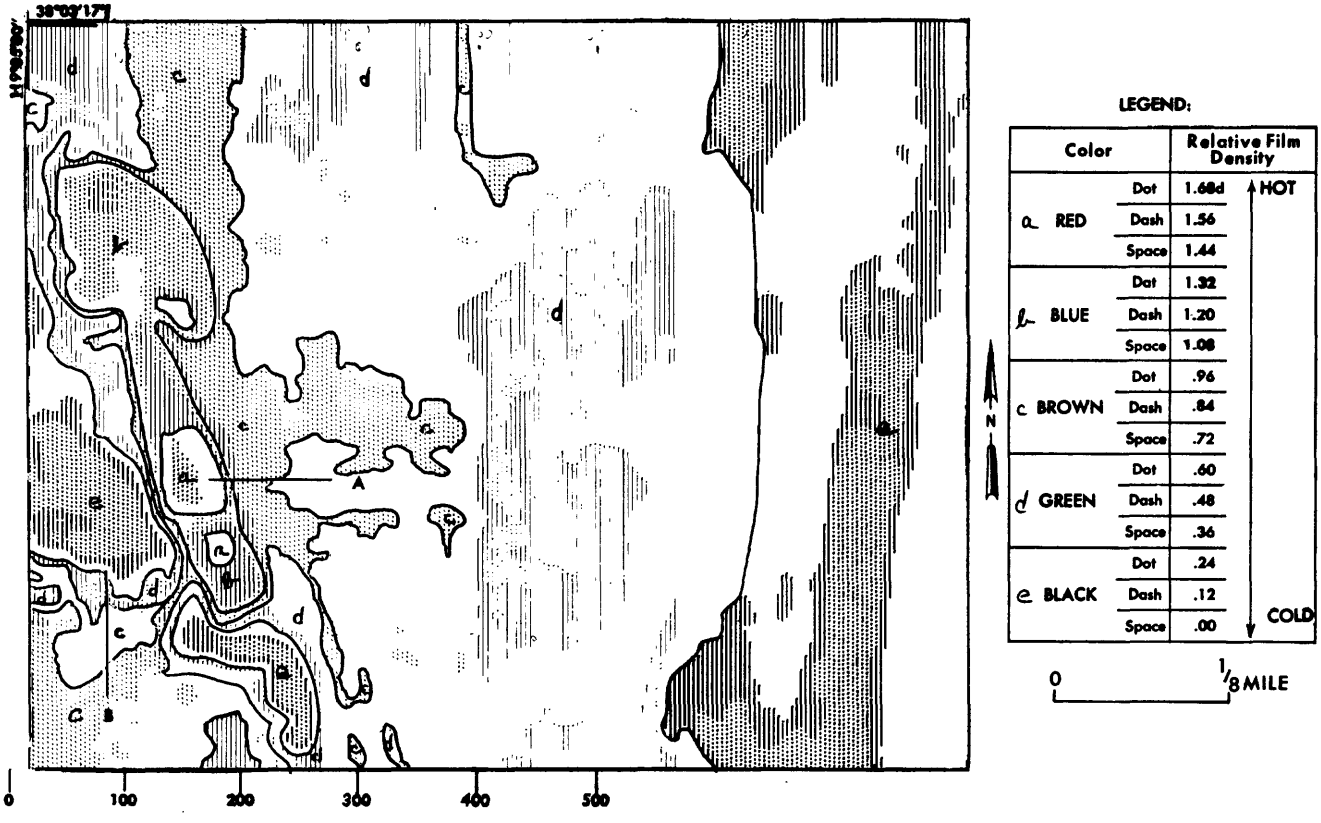

Figure 8

Figure 9. Northeastern Paoha Island: (a^1) is a salt pan in the pit of a pyroclastic crater; (b^1) Mono Lake water; (c^1) unconsolidated material and vegetation; (d^1) lacustrine tuffaceous marl; (e^1) andesite-basalt flow; and (f^1) andesite-basalt pyroclastics.

ISODENSITY SCAN OF IR IMAGERY: NORTHEASTERN PAOHA ISLAND, CALIFORNIA

7/27/66 2010 HOURS LINE 2 10 X MAGNIFICATION

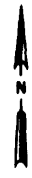

LEGEND

Color		Relative Film Density	
a RED	Dot	1.31d	↑ HOT
	Dash	1.20	
	Space	1.08	
b BLUE	Dot	.96	
	Dash	.84	
	Space	.72	
c BROWN	Dot	.60	
	Dash	.48	
	Space	.36	
d GREEN	Dot	.24	
	Dash	.12	
	Space	0.00	↓ COLD

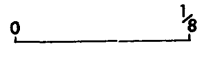

Figure 9

Figure 10. Northeastern Paoha Island: isodensity scan of post-sunset imagery shows thermal distinctions between a^1) mark (Qm), b^1) andesite-basalt flows (QPva) and c^1) Mono Lake.

ISODENSITY SCAN OF IR IMAGERY: NORTHEASTERN PAOHA ISLAND, CALIFORNIA

7/27/66 2038 HOURS LINE 2 10 X MAGNIFICATION

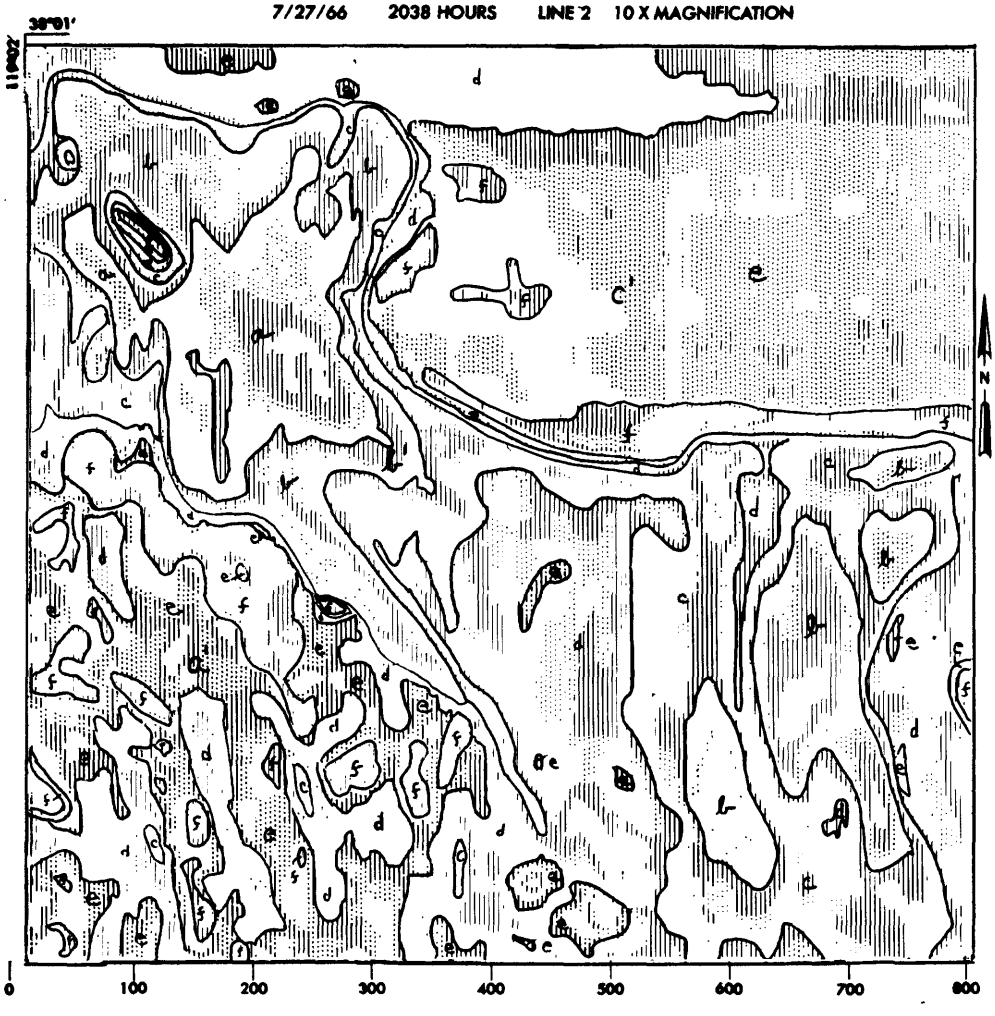

LEGEND

Color		Relative Film Density	
a RED	Dot	.67d	HOT
	Dash		
	Space	.59	
b BLUE	Dot	.55	
	Dash	.51	
	Space	.47	
c BROWN	Dot	.43	
	Dash	.40	
	Space	.36	
d GREEN	Dot	.32	
	Dash	.28	
	Space	.24	
e BLACK	Dot	.20	
	Dash	.16	
	Space	.12	
f PURPLE	Dot	.08	
	Dash	.04	
	Space	.00	COLD

0 1/8 MILE

Figure 10

Figure 11. Northeastern Paoha Island: isodensity scan showing virtual disappearance of radiant-temperature distinctions between most lithologic units (e.g., a^1 & b^1) by 4:07 a.m., July 28, 1966, compared to 8:00 p.m. imagery, with the exception of the residual anomaly at (c^1) correlated with the position of andesite-basalt flow ridge. Note the reversal in comparative temperature position of Mono Lake (d^1): Lake water exhibits higher radiance at this predawn hour than bedrock or unconsolidated materials.

ISODENSITY SCAN OF IR IMAGERY: NORTHEASTERN PAOHA ISLAND, CALIFORNIA

7/28/66 0407 HOURS LINE 2 10× MAGNIFICATION

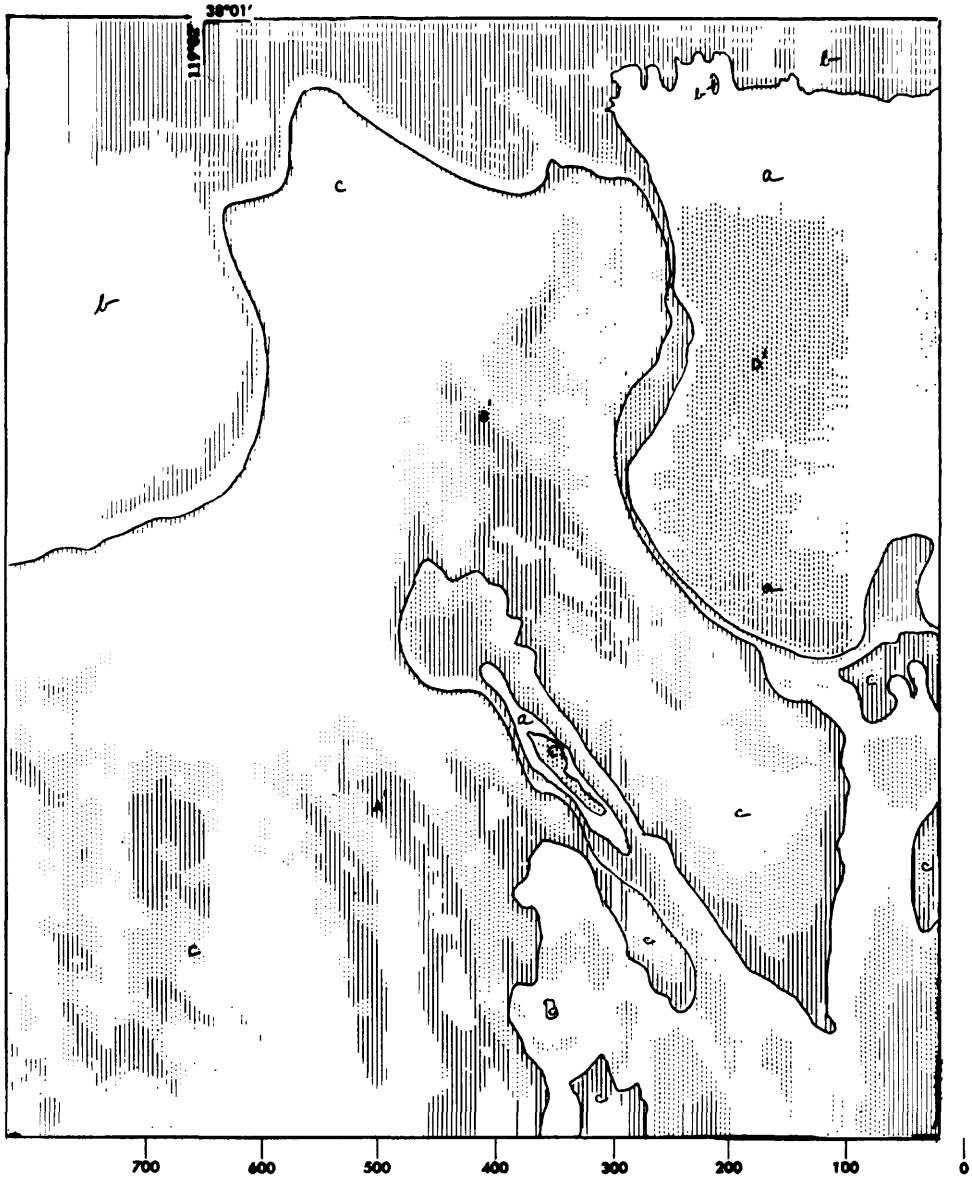

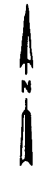

LEGEND

Color		Relative Film Density	
a RED	Dot	.96d	HOT
	Dash	.84	
	Space	.72	
b BLUE	Dot	.60	
	Dash	.48	
	Space	.36	
c BROWN	Dot	.24	
	Dash	.12	
	Space	.00	COLD

0 1/8 MILE

Figure 11

Figure 12. Eastern Paoha Island: area of lowest radiance (a^1) is a thickly vegetated beach deposit; (b^1) is a hummocky area of lacustrine marl (Qm); (c^1) Mono Lake; (d^1) andesite-basalt volcanics (Qpva); and (e^1) a thermal spring area barely distinguishable on this scan in which only 12 isodensity units are used.

ISODENSITY SCAN OF IR IMAGERY: EASTERN PAOHA ISLAND, CALIFORNIA

7/27/66 2010 HOURS LINE 2 10 X MAGNIFICATION

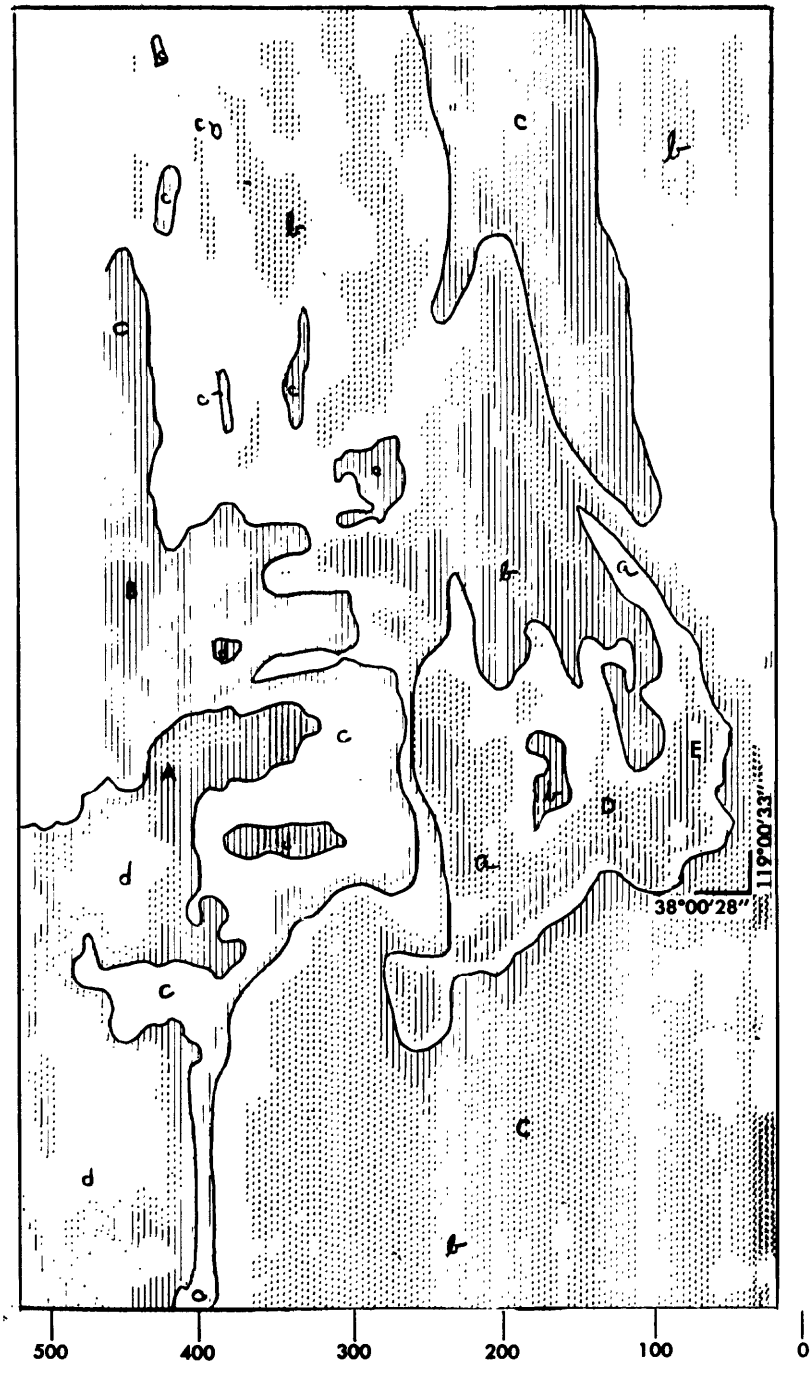

LEGEND

Color		Relative Film Density
a RED	Dot	HOT
	Dash	
	Space	1.08d
b BLUE	Dot	.96
	Dash	.84
	Space	.72
c BROWN	Dot	.60
	Dash	.48
	Space	.36
d GREEN	Dot	.24
	Dash	.12
	Space	.00 COLD

N

0 1/8 MILE

Figure 12

Figure 13. Eastern Paoha Island: utilization of 21 isodensity units permits delineation of five thermal anomalies as distinct from normally warm andesite-basalts which appear as units of lower density.

ISODENSITY SCAN OF IR IMAGERY: EASTERN PAOHA ISLAND, CALIFORNIA
7/27/66 2038 HOURS LINE 2 10 X MAGNIFICATION

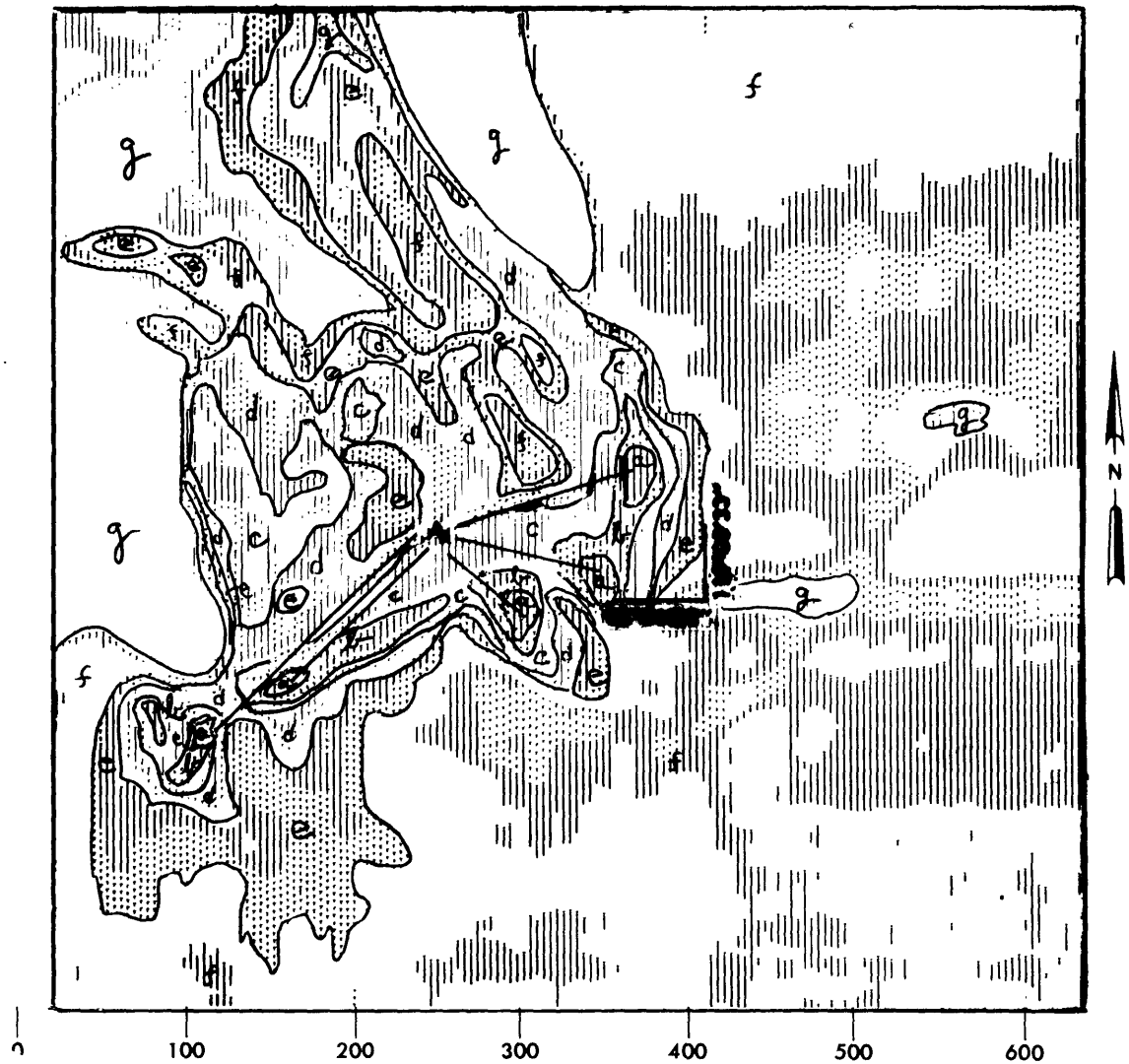

LEGEND

Color		Relative Film Density	
a RED	Dot	.79d	HOT
	Dash	.75	
	Space	.71	
b BLUE	Dot	.67	
	Dash	.63	
	Space	.59	
c BROWN	Dot	.55	
	Dash	.51	
	Space	.47	
d GREEN	Dot	.43	
	Dash	.40	
	Space	.36	
e BLACK	Dot	.32	
	Dash	.28	
	Space	.24	
f PURPLE	Dot	.20	
	Dash	.16	
	Space	.12	
g TURQUOISE	Dot	.08	
	Dash	.04	
	Space	.00	COLD

N

0 1/8 MILE

Figure 13

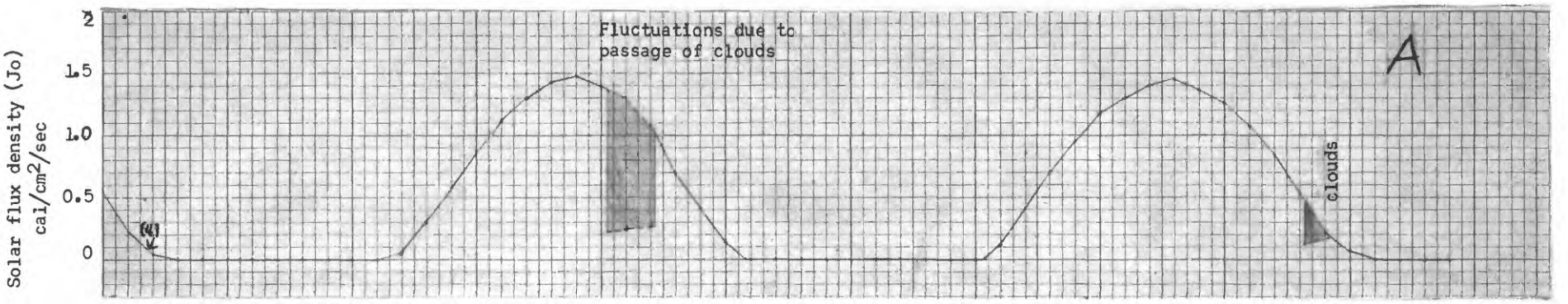

Figure 14A. Incident radiant solar flux Mono Lake,
July 27 and 28, 1966

(4) Eppley pyranometer on shed roof, South Beach Station,
Mono Craters registers solar flux in cal/cm^2/sec

Figure 14B - Explanation

(1) Tempscribe No. 9 in near-surface water of large pond SW 100' from building, at Black Point Hot Spring (deviation 20∠) - middle pond

(2) Thermograph No. 2, ambient temperature Mono Craters

(3) Tempscribe in northernmost Hot Spring pond (12th effluent)

(4) Eppley pyranometer on shed roof, South Beach Station, Mono Craters registers solar flux in cal/cm^2/sec (fig. 14A)

(5) Black Point Station thermistor probe No. 1 Qvb

(6) " " " " " No. 2 Qm

(7) " " " " " No. 3 Qal

(8) " " " " " No. 4 Qvb

(9) " " " " " No. 5 Qm

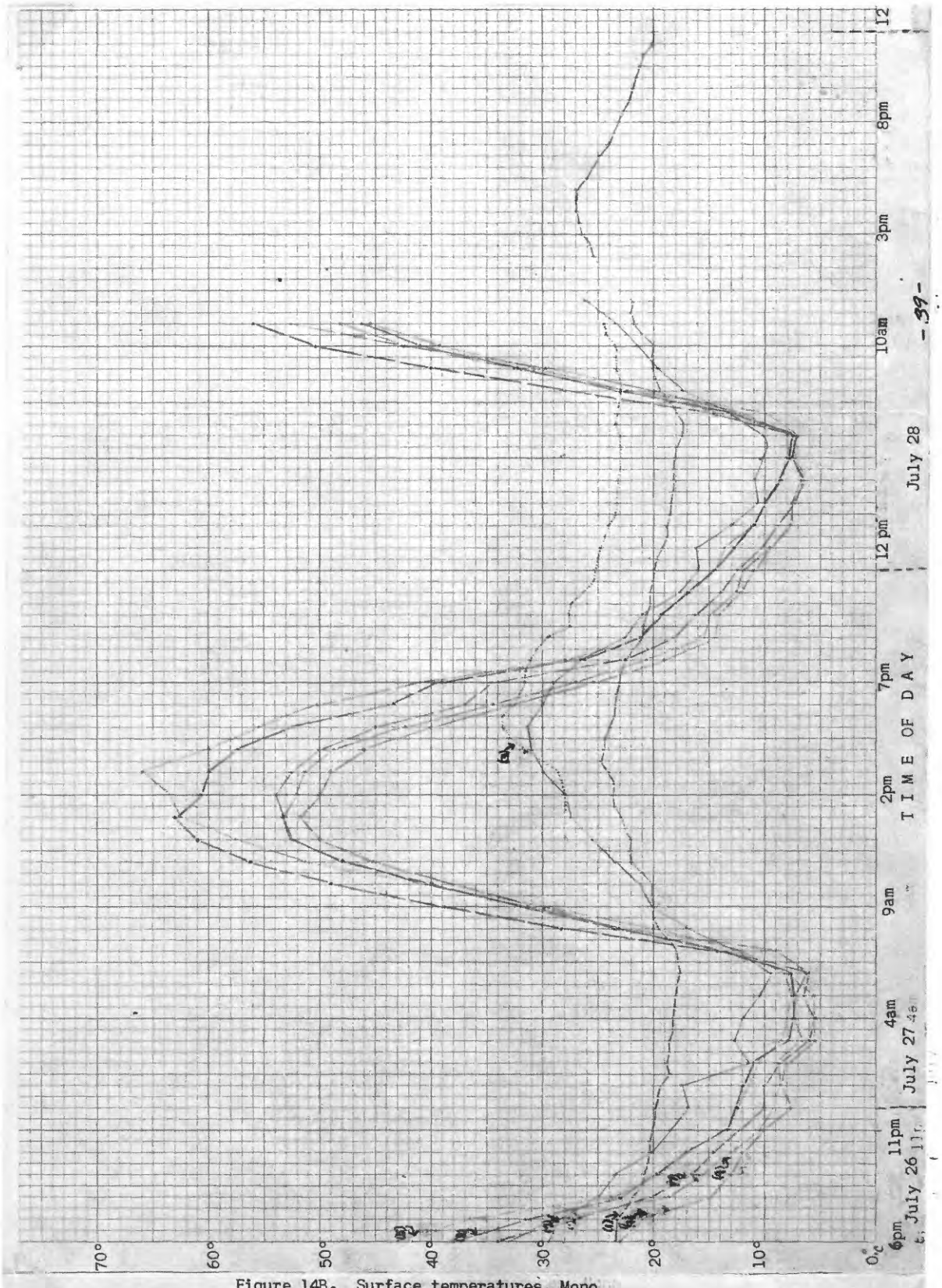

Figure 14B. Surface temperatures, Mono Instrument Stations, July 27 and 28, 1966

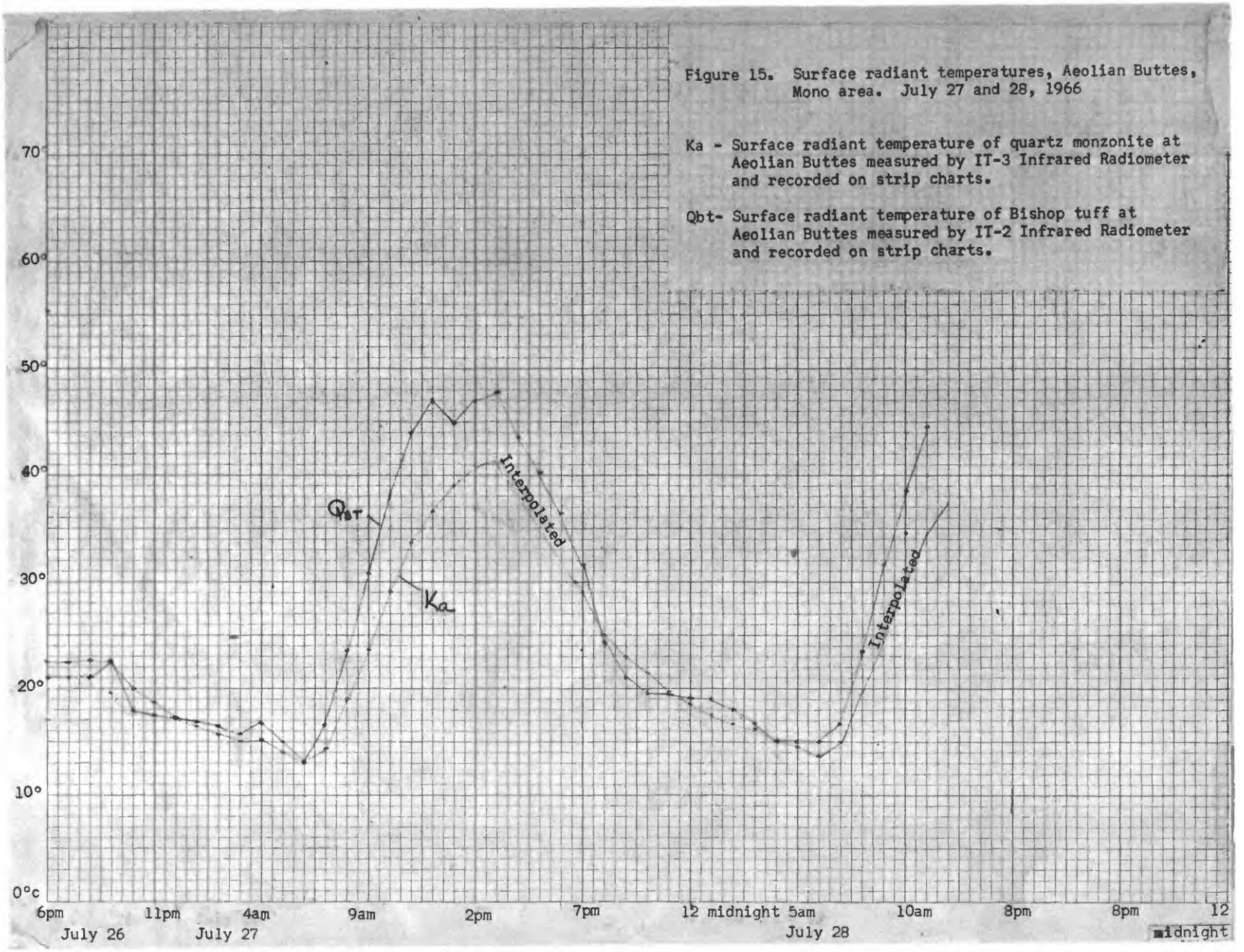

Figure 15. Surface radiant temperatures, Aeolian Buttes, Mono area. July 27 and 28, 1966

Ka - Surface radiant temperature of quartz monzonite at Aeolian Buttes measured by IT-3 Infrared Radiometer and recorded on strip charts.

Qbt- Surface radiant temperature of Bishop tuff at Aeolian Buttes measured by IT-2 Infrared Radiometer and recorded on strip charts.

Figure 16 - Mono South Beach Station, July 27 & 28, 1966
Surface and near-surface temperatures, determined by thermistor probe.

Probe 1, No. 2012 Qp Rhyolitic pumiceous sand dune surface-depth of 1/8"±

Probe 2, No. 2042 Qp Rhyolitic pumiceous sand 4" depth

Probe 3, No. 2011 Qp Rhyolitic pumiceous sand surface

Probe 4, No. 2020 Qb Surface of slab of cemented pebbles (cement $CaCO_3$)

Probe 5, No. 2049 Qp Free air probe 4" below surface

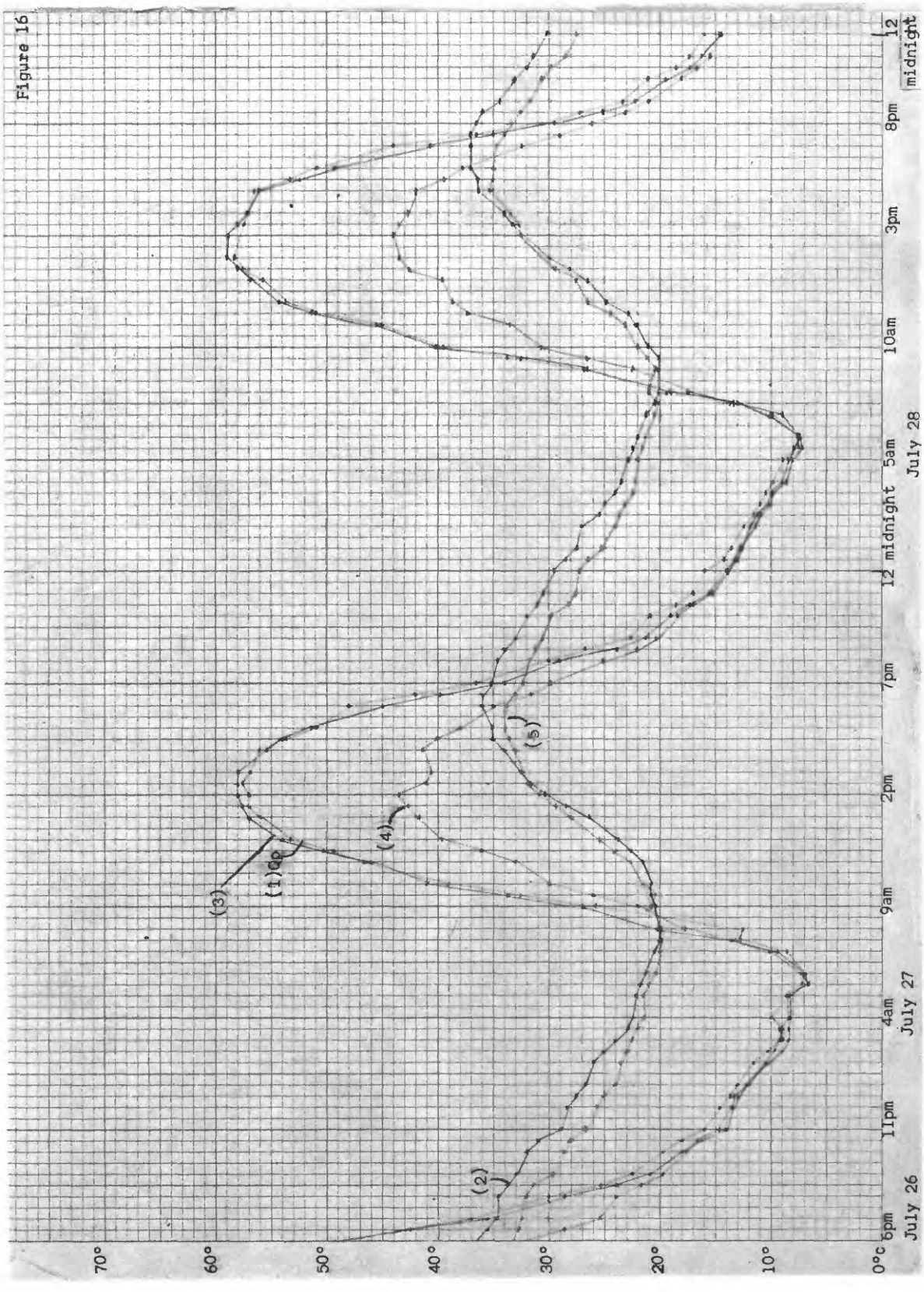
Figure 16
70°
60°
50°
40°
30°
20°
10°
0°c
6pm
July 26
11pm
4am
July 27
9am
2pm
7pm
12 midnight
5am
July 28
10am
3pm
8pm
12
midnight
(1)
(2)
(3)
(4)
(5)

Figure 17 - Change of temperature with depth, July 26-28, East pumice sand flat, Monitoring Station, Mono area

Qp (1) Thermistor probe at surface of pumice sand

Qp (2) Thermistor probe at depth of 1"

Qp (3) Thermistor probe at depth of 2"

Qp (4) Thermistor probe at depth of 3"

Qp (5) Thermistor probe at depth of 4"

Instrument Station No. 3 - Variable sequencer No. G 258931

Figure 17

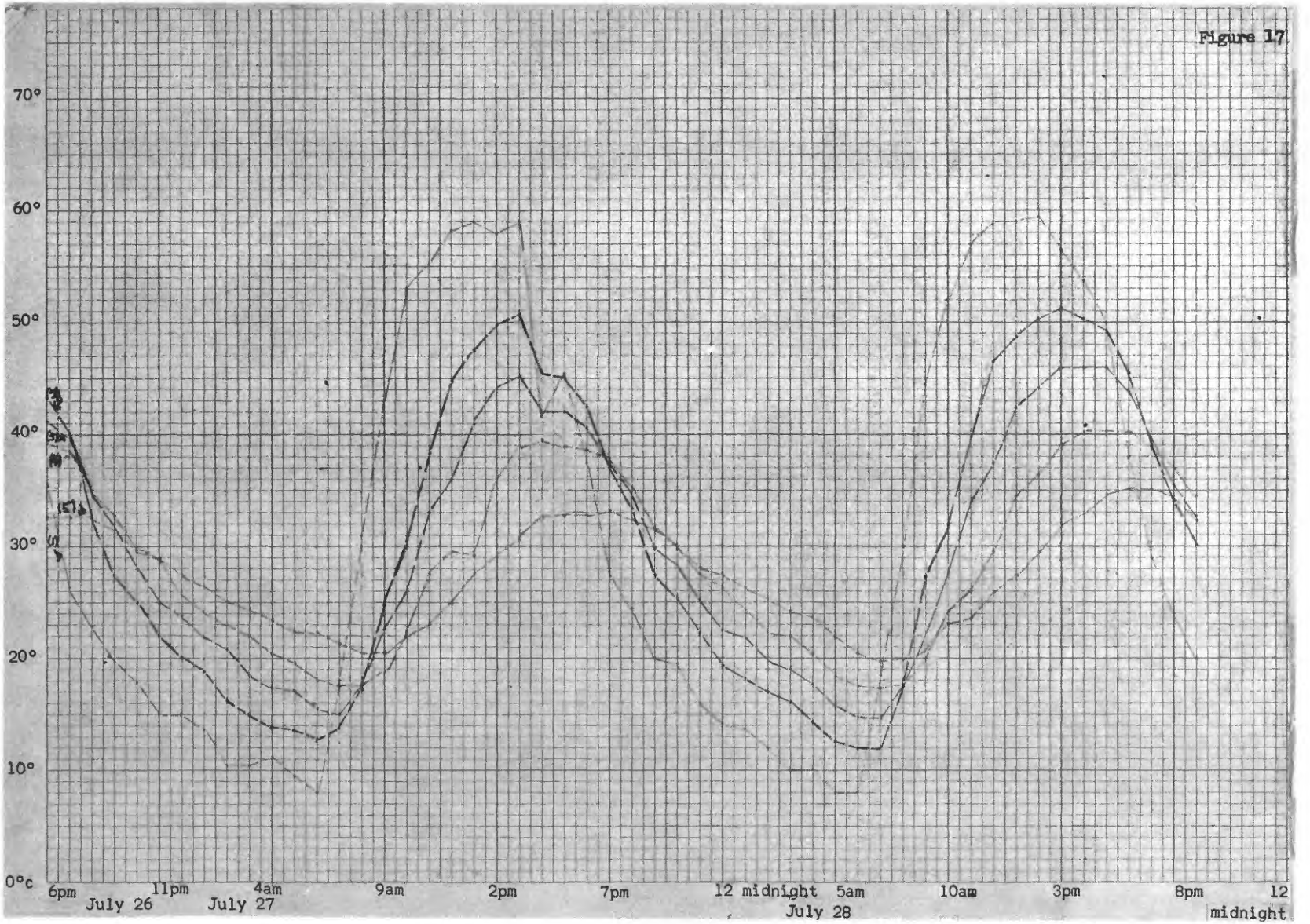
70°
60°
50°
40°
30°
20°
10°
0°c
6pm
July 26
11pm
4am
July 27
9am
2pm
7pm
12 midnight
July 28
5am
10am
3pm
8pm
12
midnight

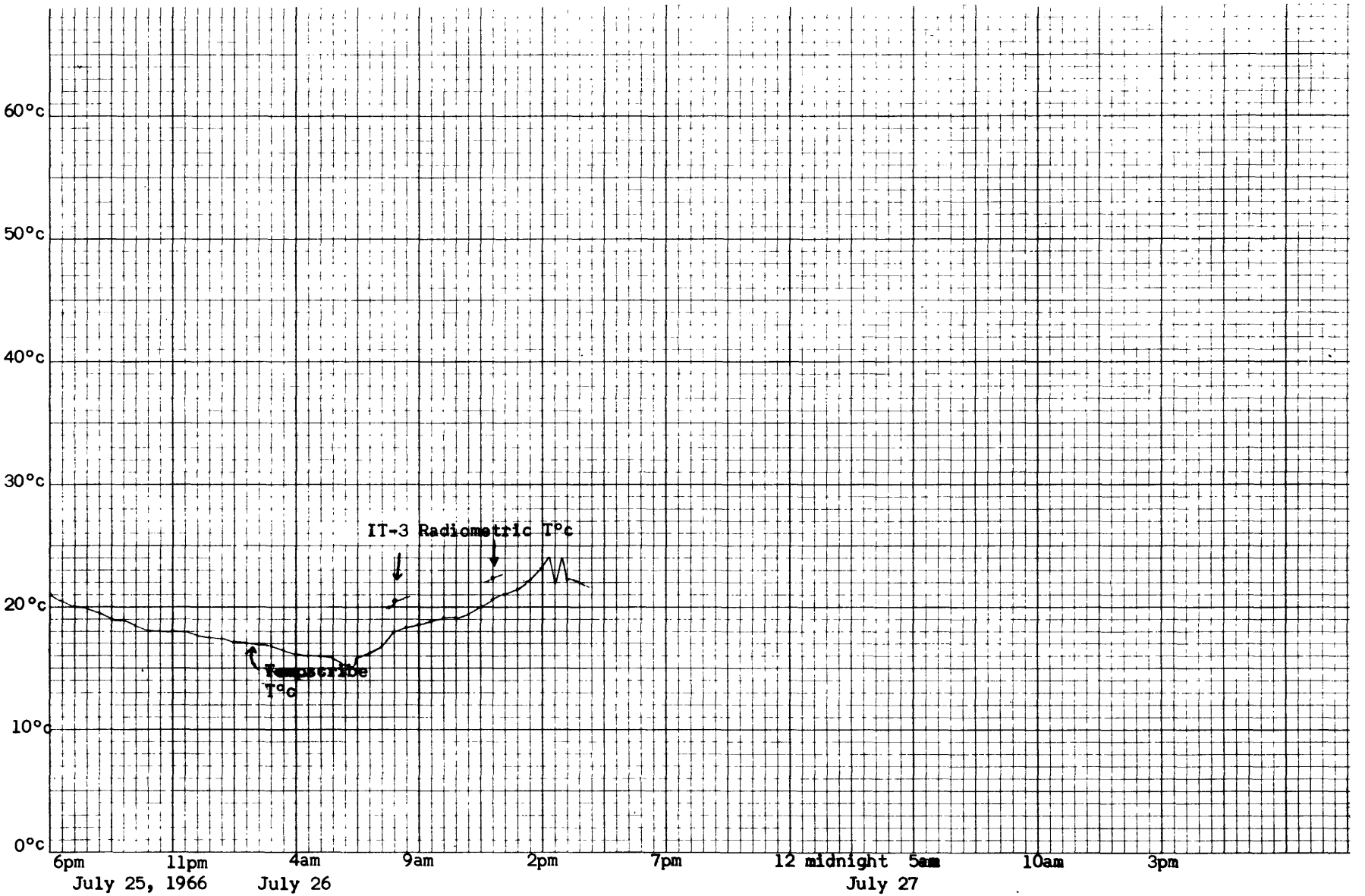

Figure 18 - Surface temperature of Mono Lake
South Beach area 120' out in 3' depth at 6" below surface (tempscribe)

Figure 19. IR image density in relation to surface temperature Black Point, Mono Lake, California, July 27-28, 1966. Determined from isodensity scans of infrared imagery.

△ Qpbp or Qvb — Lapilli-ash basalt Pyroclastics

▲ Qal — Silty deltaic and channel deposits

o Qm — Lacustrine carbonate deposits

● Mono Lake Water

□ Hot Spring Effluent, Black Point

(1) 7/27/66 0750 hours Wilson Creek Delta, Black Point
(2) 7/27/66 1233 hours Wilson Creek Delta, Black Point
(3) 7/27/66 1233 hours Deschambeau Ranch, Black Point
(4) 7/27/66 1631 hours Wilson Creek Delta, Black Point
(5) 7/27/66 1631 hours Deschambeau Ranch, Black Point
(6) 7/27/66 2008 hours Wilson Creek Delta, Black Point
(7) 7/27/66 2008 hours Deschambeau Ranch, Black Point
(8) 7/27/66 2359 hours Wilson Creek Delta, Black Point
(9) 7/27/66 2359 hours Deschambeau Ranch, Black Point
(10) 7/28/66 0404 hours Wilson Creek Delta, Black Point
(11) 7/28/66 0404 hours Deschambeau Ranch, Black Point

Figure 19

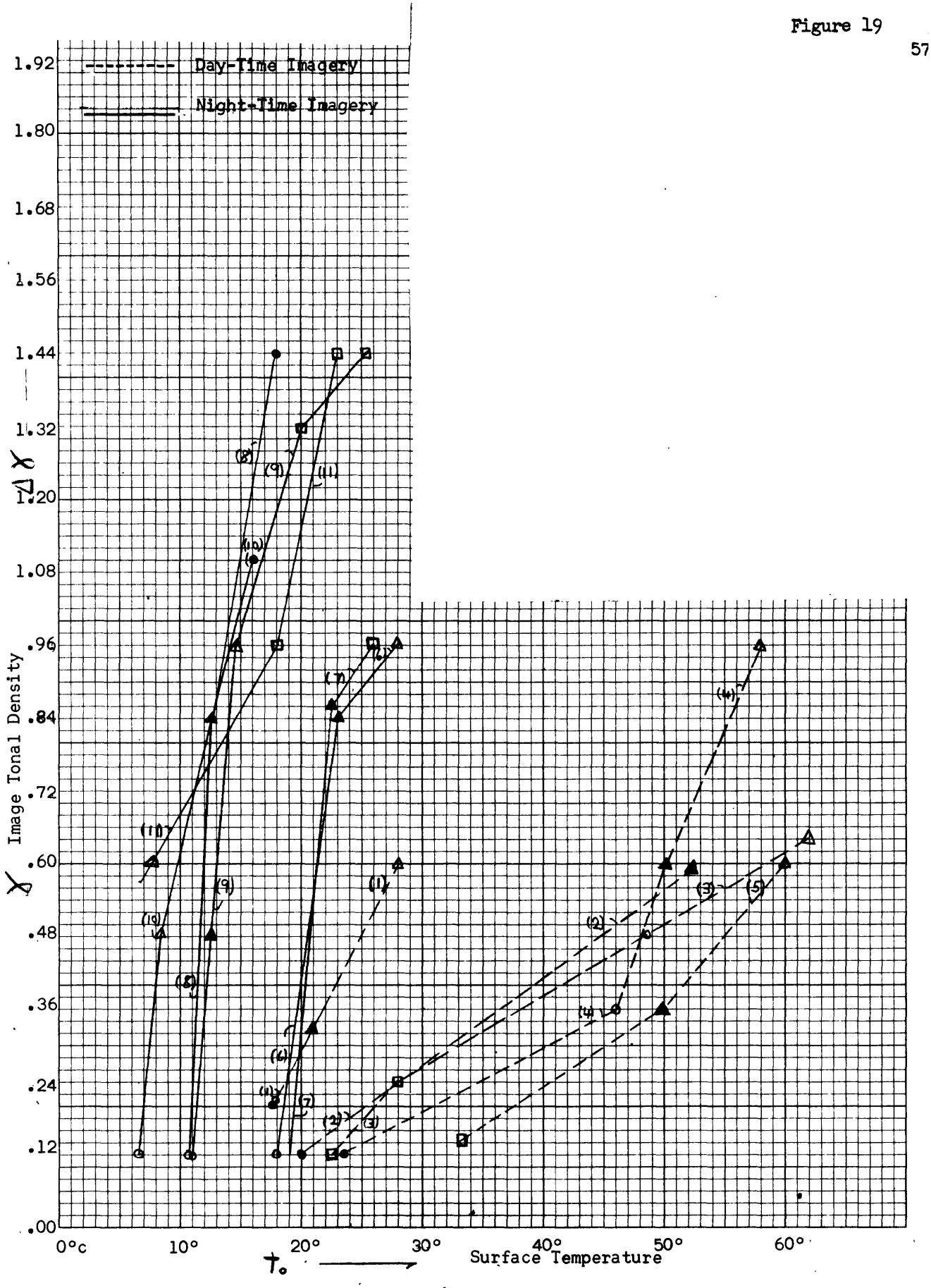
Day-Time Imagery
Night-Time Imagery
1.92
1.80
1.68
1.56
1.44
1.32
1.20
1.08
.96
.84
.72
.60
.48
.36
.24
.12
.00
γΔ
γ Image Tonal Density
0°c
10°
20°
30°
40°
50°
60°
t° Surface Temperature

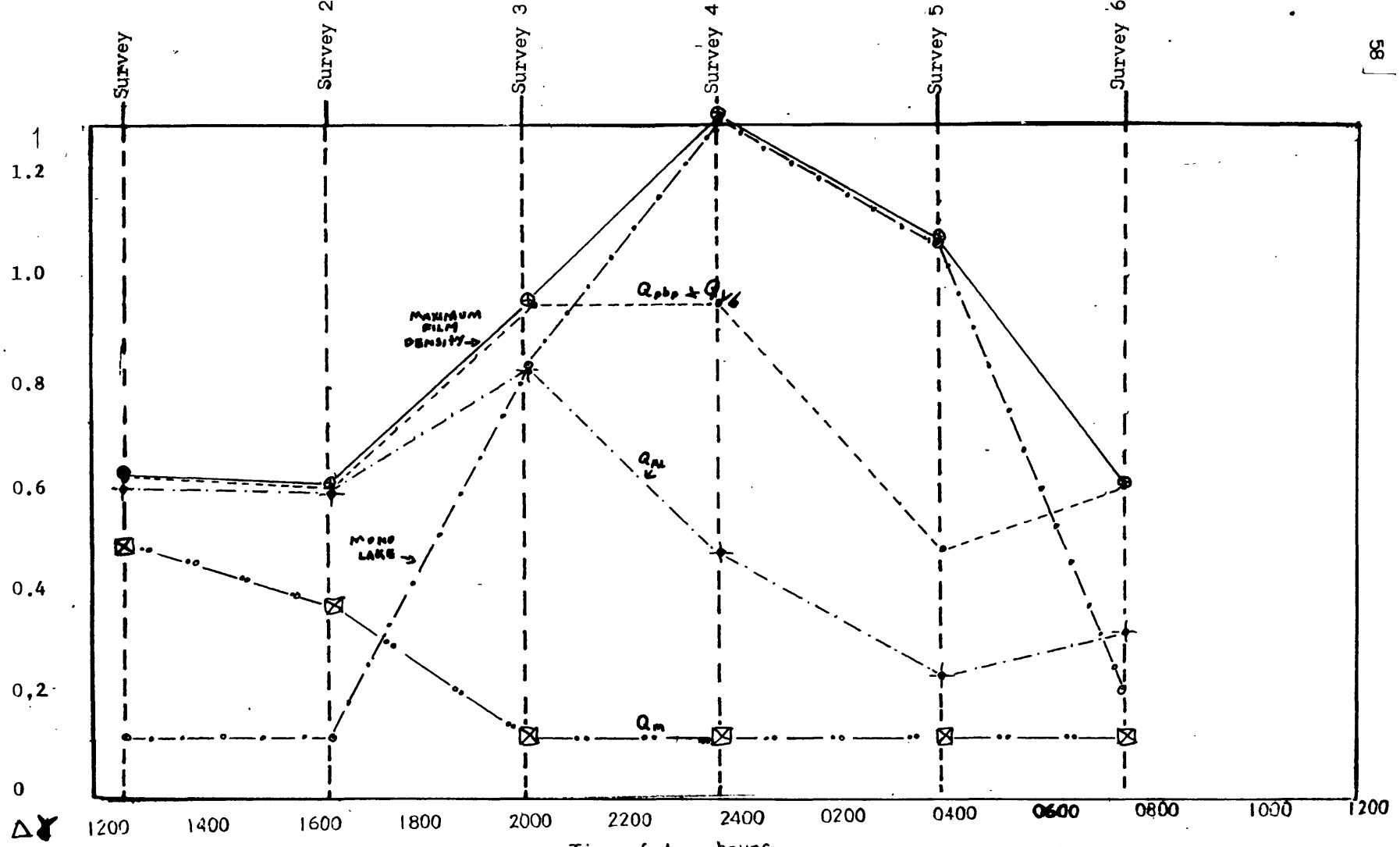

July 27 - 28, 1966
Black Point, California

Change in relative film density with time during a diurnal cycle for three lithologies and water. Film density of each material is plotted in relation to maximum film density for each of six sequences of imagery. Maximum film density is a function of changes in radiance and amplifier gain setting and to a lesser extent of film processing and isodensitometer settings. Film densities at the maximum film density line or at the 0.12 line suggest that the amplfier signal may have been near or beyond the latitude of the film.

Figure 20

Figure 21

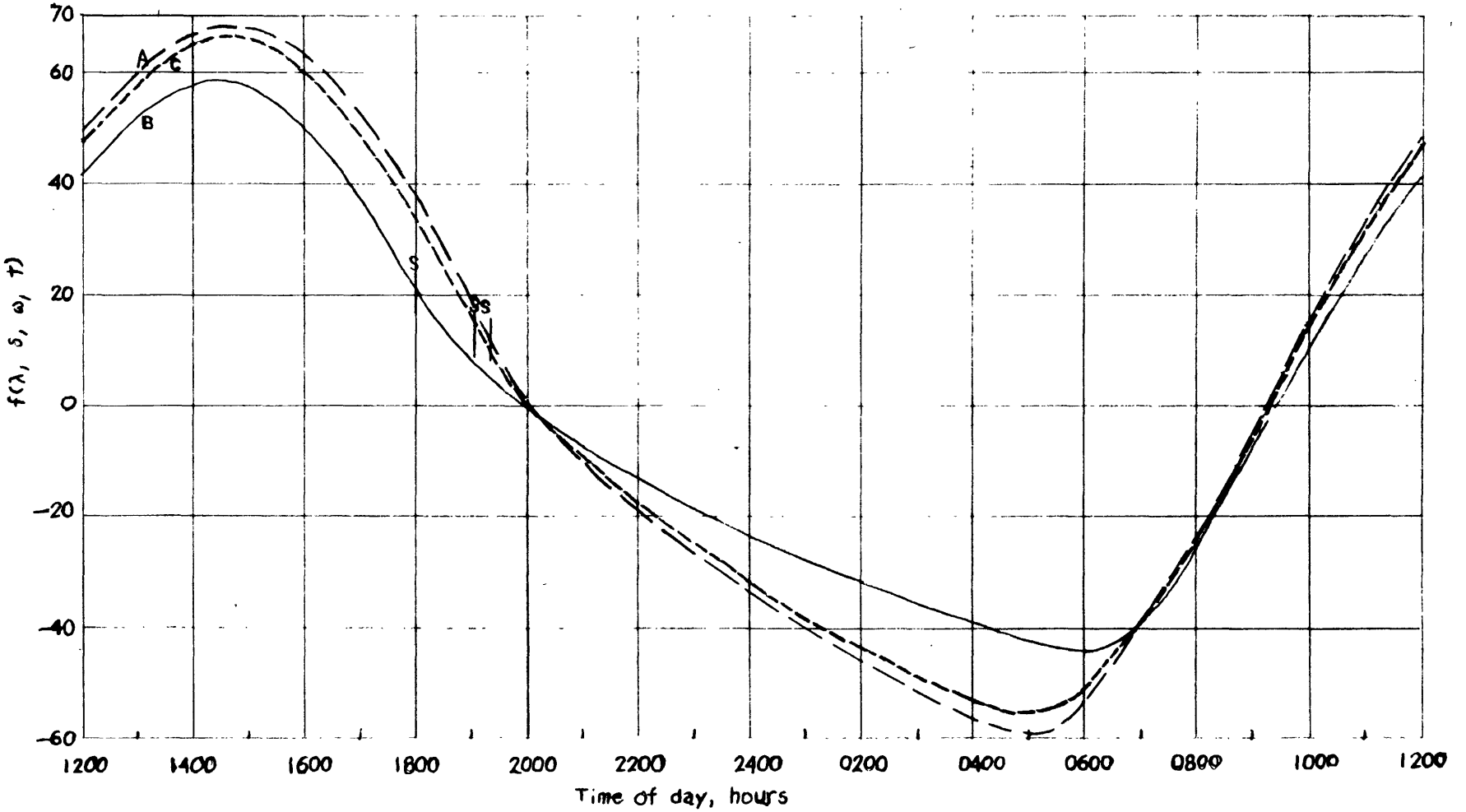

Graph of $f(\lambda, \delta, \omega, t) = \frac{\cos\lambda \cos\delta}{\omega^{1/2}} \sum_{n=1}^{\infty} \frac{2(\sin n\pi \cosh - n\cos n\pi \sinh)}{\pi n^{3/2}(n^2-1)} \cos(n\omega t - \pi/4)$

Curve A: $\delta = 23.5°$ Curve B: $\delta = 0°$ Curve C: $\delta = 19.3°$ $\lambda = 38°$
for all curves. Times of sunset are marked S.

Figure 22

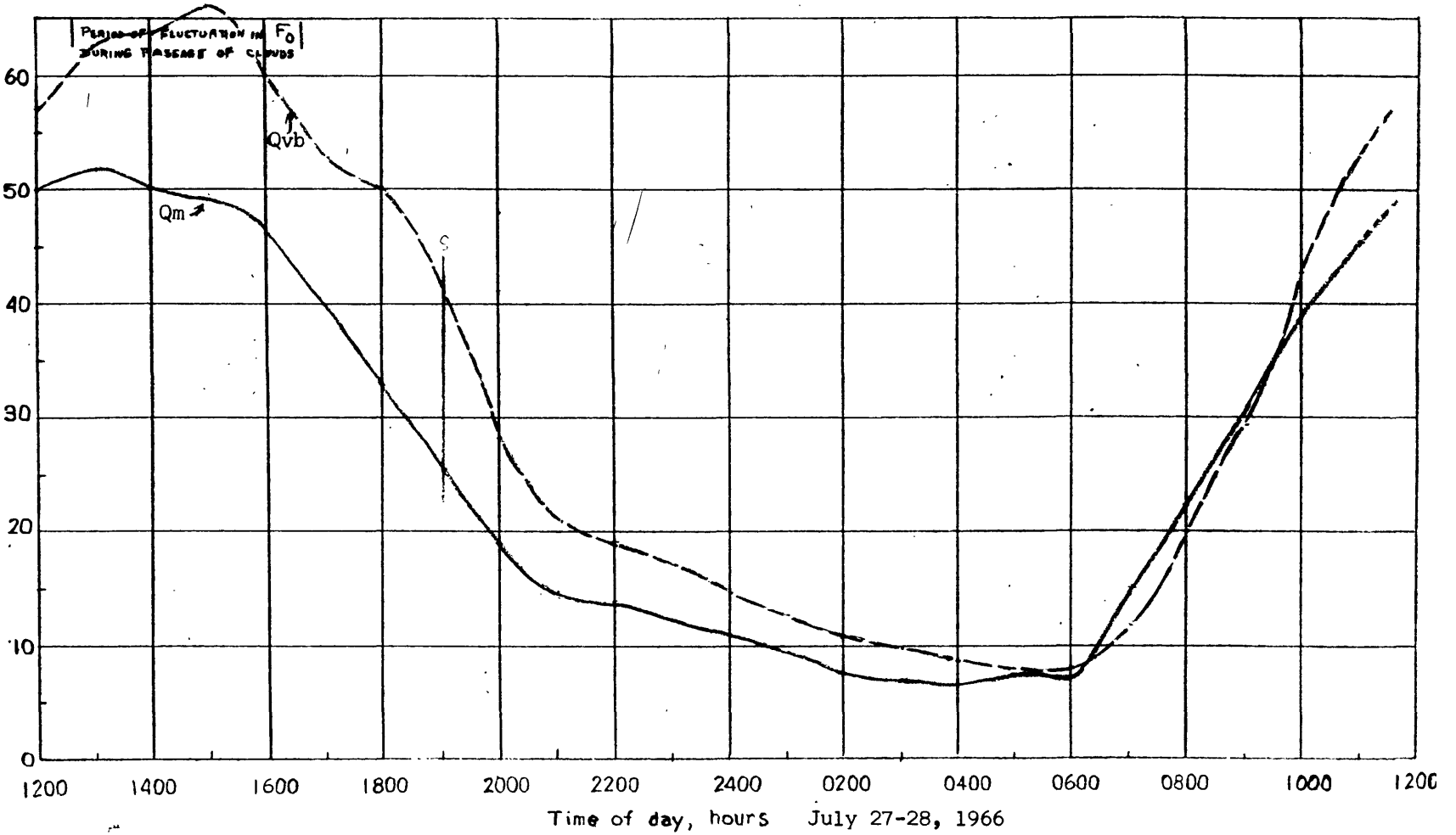

Recorded variations in apparent surface temperature with time during period of infrared survey, Black Point, California. Determined by variable sequencer - thermistor probe system. Qm is lacustrine carbonate crust and Qvb is olivine basalt lapilli-ash of Black Point. Emissivity (8-14μ) of Qm = 0.974 ± 0.002; Qvb = 0.985 ± 0.003.

Figure 23

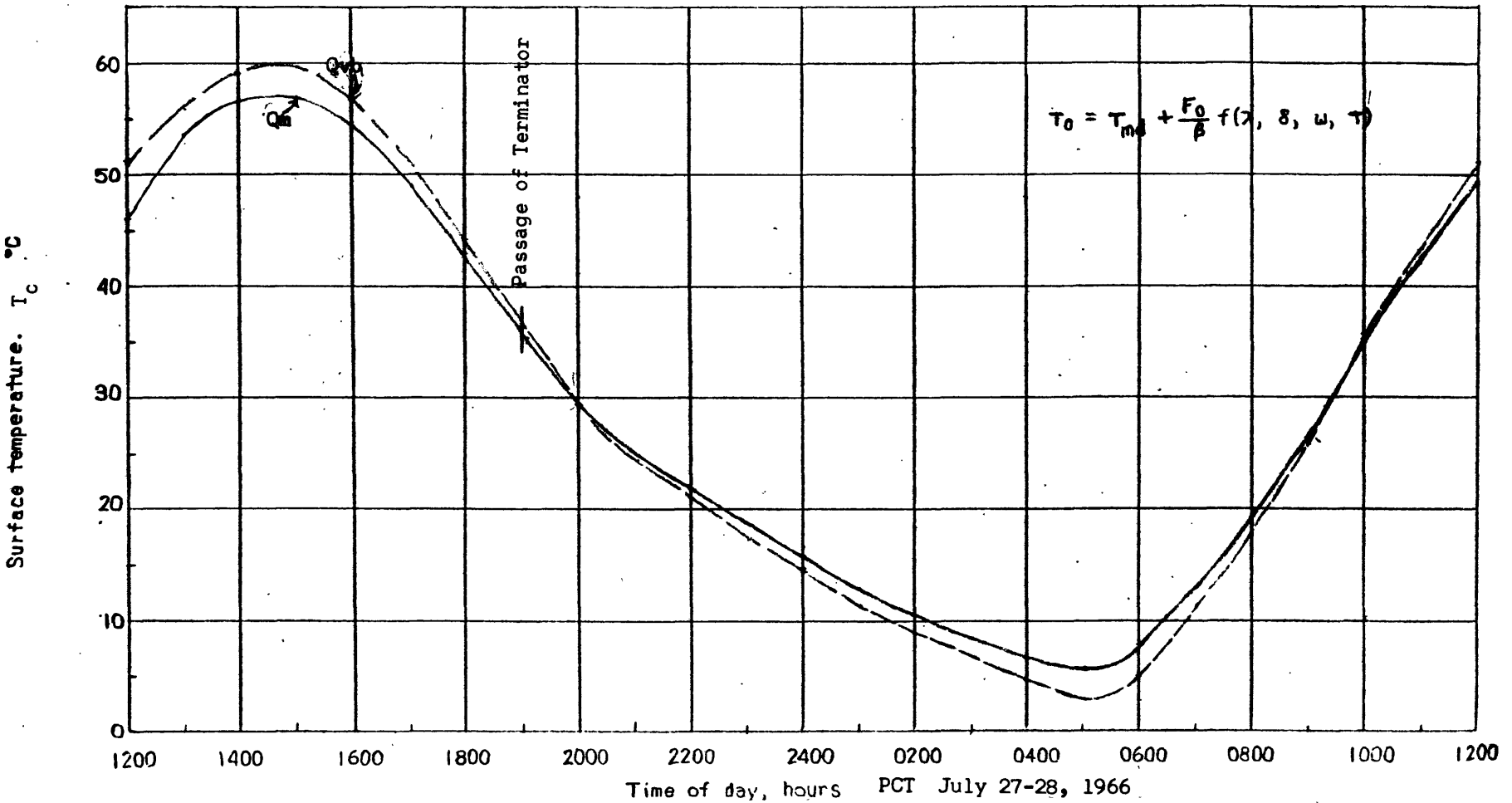

Theoretical diurnal surface temperature variations for lacustrine carbonate deposits (Qm) of Black Point, and olivine basalt lapilli-ash (Qvb) of Black Point. Tmd = 29°C, estimated coefficient of absorption of solar radiation for Qm $\simeq$ 0.2; for Qvb $\simeq$ 0.75; $F_{o_{Qm}} \simeq 0.005$ cal cm^{-2} sec^{-1}; $F_{o_{Qpbp}} \cong 0.17$ cal cm^{-2} sec^{-1}; λ = 38°N; δ = 19°20'; and $\omega = \frac{2\pi}{P}$ where P = 86.400 seconds. Values of β in CGS units are β_{Qm} = 0.011 and β_{Qvb} = 0.040.

Figure 24

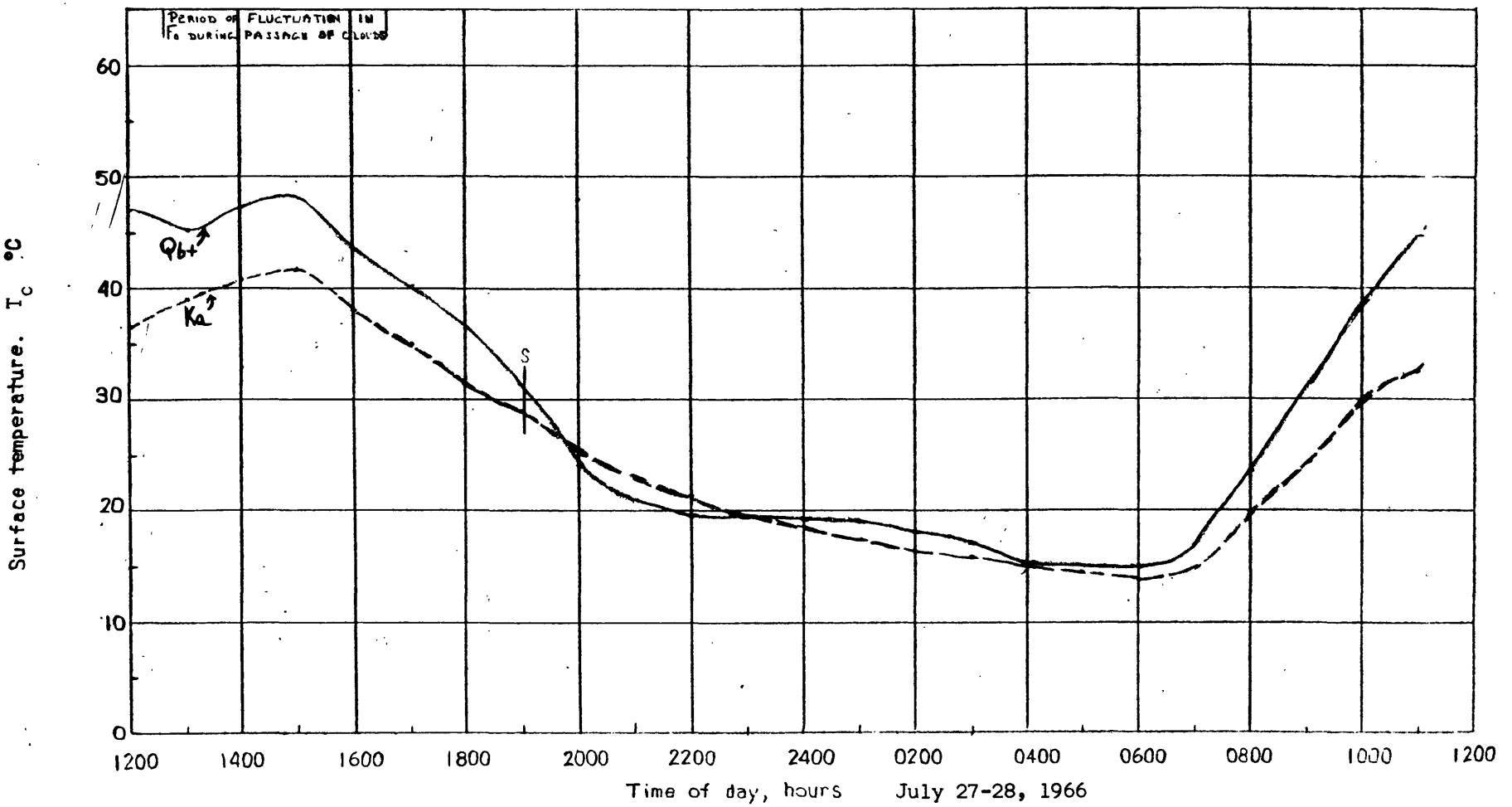

Recorded variations in blackbody-equivalent surface temperature with time during period of infrared survey, Aeolian Buttes, California. Determined by IT-3 Barnes infrared radiometers. Ka is quartz monzonite and Qbt is upper low-density unit of Bishop Tuff. Emissivity (8-14μ) of Ka = 0.932 ± 0.004; Qbt = 0.961 ± 0.002.

Figure 25

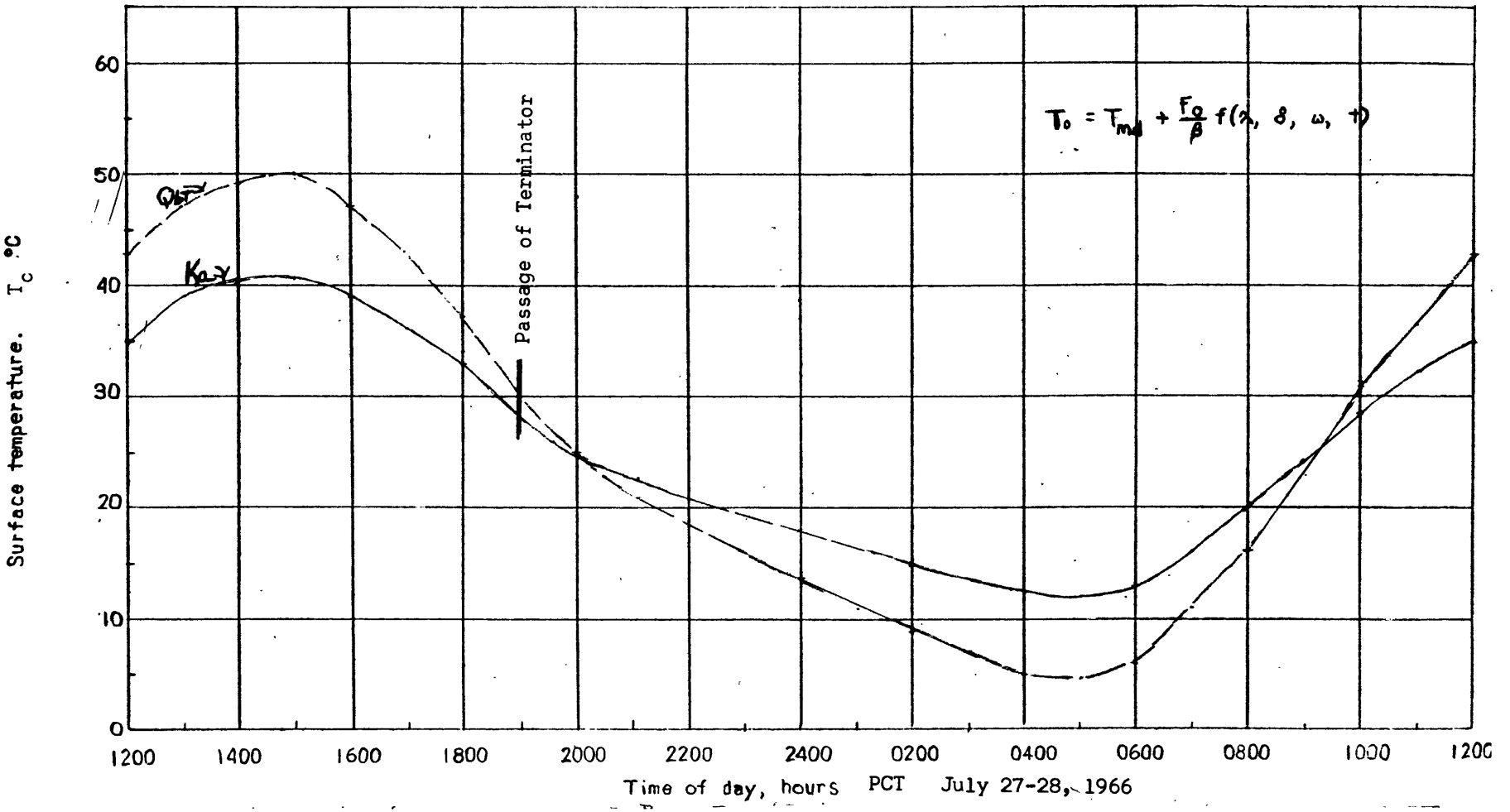

Theoretical variation in surface temperatures of upper unit of Bishop Tuff (Qbt) and quartz monzonite (Ka) of Aeolian Buttes. Tmd - 25°C. Estimated coefficient of absorption of solar radiation for both Qbt and Ka $\cong$ 0.b; $F_{o_{Qbt}} \cong 0.015$ cal cm^{-2} sec^{-1}; $F_{o_{Ka}} \cong 0.015$ cal cm^{-2} sec^{-1}; λ = 38°N; δ = 19°20'; and $\omega = \frac{2\pi}{P}$ where P = 86.400 seconds. Values of β in CGS units are $\beta_{Qbt} = 0.040$ and $\beta_{Ka} = 0.060$.

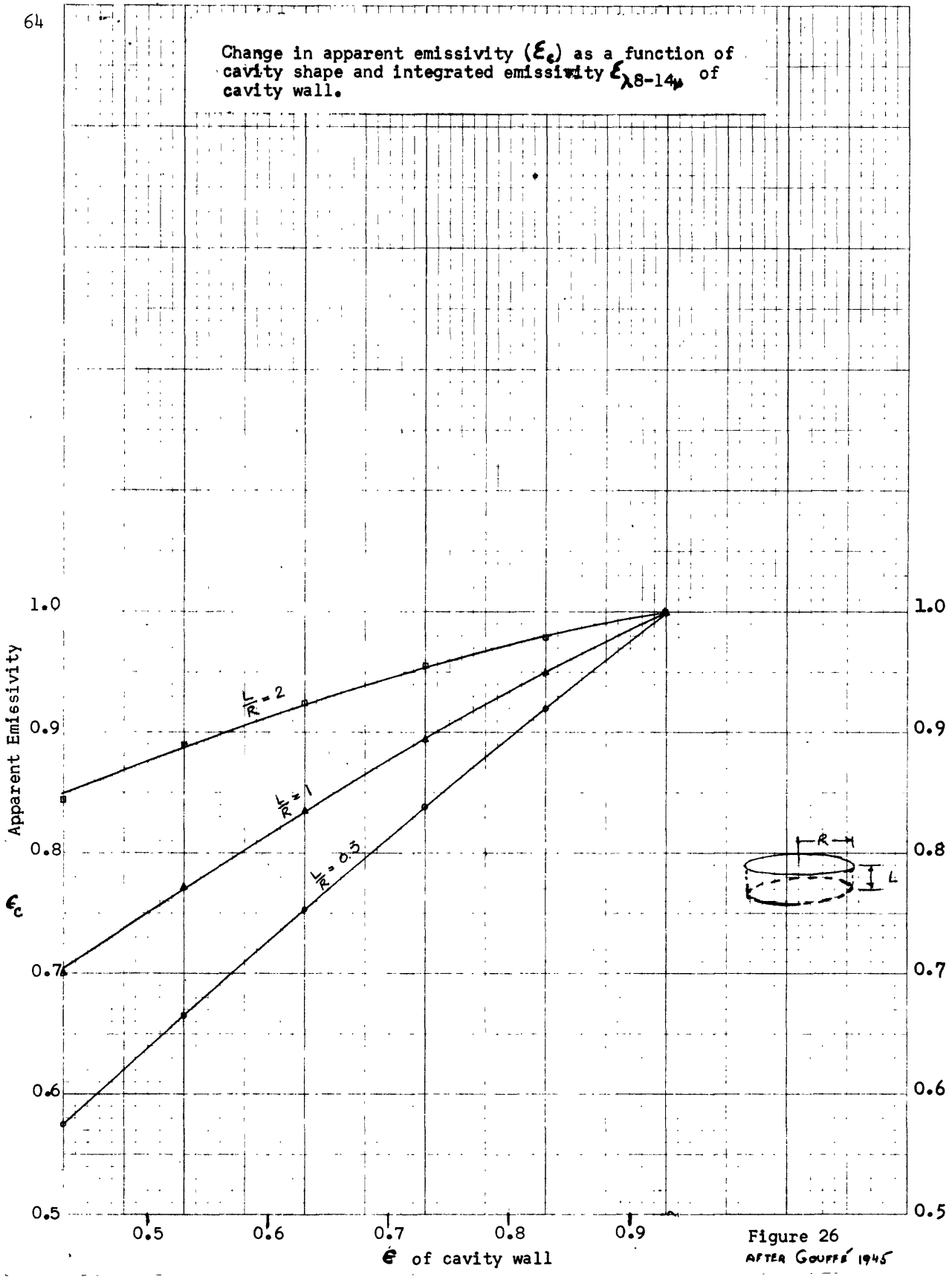

Figure 26
AFTER GOUFFÉ 1945

Figure 27. Aerial photograph of Paoha Island showing areas scanned by isodensitracer technique. Arrows on east side indicate points of thermal emission.

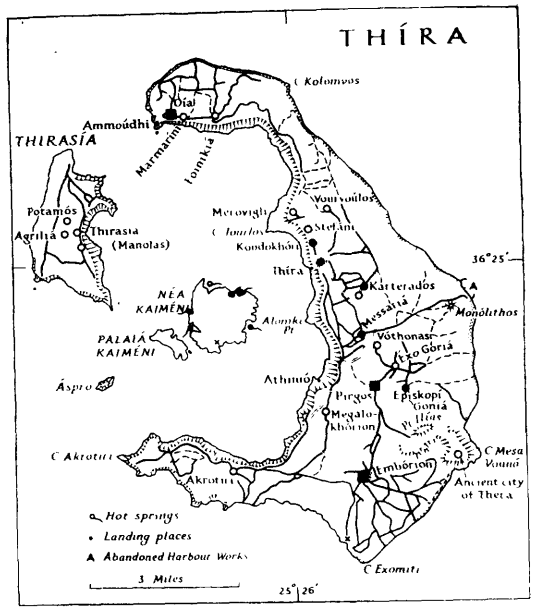

Figure 28. Subsided Santorin (Thíra) caldera in the Cyclades archipelago, Aegean Sea. Geologic features similar to Mono basin include comparable scale, comparable recency of caldera subsidence and late-volcanic stage emergence of central island craters with Néa and Palaiá Kaïméni analogous to Paoha and Negit Islands. There have also been parallel inward shifts of focus of volcanic activity with time toward Néa Kaïméni and Paoha, somewhat similar lithologies (Néa Kaïméni has andesitic. Paoha andesitic-basaltic volcanic products), similar widespread tephra layers resulting from earlier pyroclastic eruptions and similar late-stage distribution of convective thermal anomalies peripheral to the central islands.

TABLE 1

Ground Instrument Station	Flightline	Geologic Map Units	Observations	Instruments	Figure No. (This Report)
No. 1 Wilson Creek Delta, Black Point	No. 1	Qrb Qb (=Qal / Qm)	Diurnal surface Temp. variations (Contact temp.)	Multiple Thermistor-probe variable sequencer (Sprinkle)	14
No. 1A Thermal Ponds Black Point	No. 1		Thermal spring & effluent temp.	Tempscribe	
No. 2 Aeolian Buttes	No. 1	Ka Qbt Surficial pumice tephra	Diurnal radiometric surface temp variations	IT-2 IT-3 Barnes IR thermometers	15
No. 3 South Beach Mono Lake	No.2	Qb (includes (pumice (sand	Diurnal surface temp. variations Diurnal temp. variations at depth. (Contact temp.)	Multiple Thermistor-probe variable sequencer (Sprinkle)	17
Mono Lake surface	No. 2		Correct surface temp. (Contact temp.)	Tempscribe	18
No. 4 East Pumice Sand Flat	No. 3	Q_pA (pumice (sand	Solar flux density (diurnal variations)	Epply pyrheliometer	14
Airborne Radiometry	No. 2	Mono Lake	Radiometric surface temp. of Mono Lake	IT-3 Barnes IR Thermometer	18

Observers: S.J. Gawarecki, George Boynton, Philip Philbin, J.D. Friedman

IR LOG

Date 27 July 66 Take Off 0725 Project Mono Pilot Chapman Co-Pilot Simpson Scanner Type Rec. IV

Landing 0924 Airport Bishop, Calif. IR Crew Fross/Turner

Run	Mark	Heading	Line No.	Time On	Time Off	Filter 8-14μ	AGC	Alt. (MSL)	Remarks
1	5	N	1			x	Minimum	10.5M	Dry sun
2	4	S	1	0758	0805	x	"	"	
3	3	N	2	0811	0818	x	"	"	
4	2	S	3	0822	0829	x	"	"	
5	5	N	1	0833	0838	x	"	"	
6	4	S	2	0840	0848	x	"	"	
7	3	N	3	0850	0857	x	"	"	

TABLE 2 (cont'd)

IR LOG

Date 27 July 66 Take Off 1128 Project Mono Pilot Chapman Co-Pilot Simpson Scanner Type Rec. IV.

Landing 1322 Airport Bishop, Calif. IR Crew Fross/Turner

Run	Mark	Heading	Line No.	Time On	Time Off	Filter 8-14μ	AGC	Alt. (MSL)	Remarks
1	5	S	1	1157	1204	x	Minimum	10.5M	Signal excessive; reduced
2	4	N	2	1207	1215	x	"	"	bias five complete turns
3	3	S	3	1217	1225	x	"	"	improvement but still bottom-
4	2	N	1	1228	1234	x	"	"	ing. Scope shows some noise
5	5	S	2	1236	1244	x	"	"	in water, Wea. clear, air rough,
6	4	N	3	1246	1253	x	"	"	some clouds over lake.
	3	FINISH -	PRINTED - WARM-UP						

TABLE 2 (cont'd)

IR LOG

Date 27 July 66 Take Off 1530 Project Mono Pilot Chapman Co-Pilot Simpson Scanner Type Rec. IV.

Landing 1722 Airport Bishop, Calif. IR Crew Fross/Turner

Run	Mark	Heading	Line No.	Time On	Time Off	Filter 8-14μ	AGC	Alt. (MSL)	Remarks
1	5	S	1	1603	1610	x	Minimum	10.5M	Much signal ↳ reduced bias ↳
2	4	N	2	1612	1619	x	"	"	still bottoming; light clouds
3	3	S	3	1620	1629	x	"	"	over lake - clear visibility
4	2	N	1	1631	1638	x	"	"	a rough ride.
5	5	S	2	1641	1646	x	"	"	
6	4	N	3	1647	1655	x	"	"	
	3	FINISH AND WARM-UP							

TABLE 2 (cont'd)

IR LOG

Date 27 July 66 Take Off 0936 Project Mono Pilot Rote Co-Pilot Hegel Scanner Type Rec. IV.

Landing _____ Airport Bishop, Calif. IR Crew Fross/Turner

Run	Mark	Heading	Line No.	Time On	Time Off	Filter 8-14μ	AGC	Alt. (MSL)	Remarks
1	5	N	1	2003	2008	x	3	10.5M	AGC/3/bias - 2
2	4	S	2	2010	2017	x	"	"	
3	3	N	3	-	2027	x	"	"	
4	2	S	1	2029	2036	x	"	"	
5	5	N	2	2038	2045	x	"	"	
6	4	S	3	2046	2053	x	"	"	
	3	FINISH - PRINTED WARM-UP.							

TABLE 2 (cont'd)

IR LOG

Date 27 July 66 Take Off 2337 Project Mono Pilot Rote Co-Pilot Hegel Scanner Type Rec. IV.

Landing _____ Airport Bishop, Calif. IR Crew Fross

Run	Mark	Heading	Line No.	Time On	Time Off	Filter 8-14μ	AGC	Alt. (MSL)	Remarks
1	5	N	1	2359	0005	x	3	10.5M	
2	4	S	2	0007	0014	x	"	"	
3	3	N	3	0015	0023	x	"	"	
4	2	S	1	0025	0031	x	"	"	
5	5	N	2	0033	0040	x	"	"	
6	4	S	3	0042	0048	x	"	"	
	3	FINISH - PRINTED WARM-UP							

TABLE 2 (cont'd)

IR LOG

Date 28 July 66 Take Off 0338 Project Mono Pilot Rote Co-Pilot Hegel Scanner Type Rec. IV.

Landing _____ Airport Bishop, Calif. IR Crew Fross

Run	Mark	Heading	Line No.	Time On	Time Off	Filter 8-14μ	AGC	Alt. (MSL)	Remarks
1	5	N	1	0400	0405	x	4	10.5M	
2	4	S	2	0407	0414	x	"	"	
3	3	N	3	0415	0422	x	"	"	
4	2	S	1	0425	0430	x	"	"	
5	5	N	2	0435	0443	x	"	"	
6	4	S	3	0444	0450	x	"	"	
	3	FINISH - PRINTED WARM-UP.							

TABLE 3

INTEGRATED 8-14μ EMISSIVITIES OF ROCKS FROM MONO CRATERS REGION
(KERN-BUETTNER STYLE "EMISSIVITY BOX" - BARNES IT-3 INFRARED THERMOMETER)
MEASUREMENTS MADE AT INFRARED LABORATORY, U.S.G.S., ARLINGTON, VIRGINIA
by

David L. Daniels

$$\epsilon = \frac{I_N}{I_{BB}} = \frac{\int_{8\mu}^{14\mu} \epsilon(\lambda) B(\lambda T) d\lambda}{\int_{8\mu}^{14\mu} B(\lambda, T) d\lambda}$$

Field #	Unit	Rock Description	Location	1	2	3	4	Average
G-66-11	Qvb	Basaltic lapilli with lacustrine silt-unconsolidated	Delta Channel Black Point	.986	.982	.986	.984	.985
SF-66-18	Q_m	Lacustrine silt encrusted with evaporite salts - playa in crater	South Crater on Paoha Is.	.973	.977	.978	.974	.976
G-66-12	Q_{al}	Fragile crust of basaltic sand and lacustrine silt - unconsolidated deposit	Delta Channel Black Point	.976	.972	.972	.976	.974
328	Q_{jlb}	Red, oxidized, basalt cinder - from rim of low splatter cones-June Lake Basalt unit	One mile NE June Lake Junction	.967	.974	.973	.976	.973
F-66-13	Q_m	Unconsolidated marl - fragile crust of lacustrine silt	SE Paoha Is.	.967	.972	.972	.970	.970
F-66-16	Q_b	Fragile, calcareous, crust of lacustrine silt - unconsolidated beach deposit	Black Point (station #1)	.968	.969	.975	.968	.970
G-66-4B	Q_{bt}	Bishop Tuff-uppermost unit-tan, crystal lithic rhyolite tuff-surface rough, moderate weathering	Aeolian Buttes	.963	.984	.966	.964	.969
339	Q_{yrp}	Rhyolitic lapilli-rhyolite pumice and obsidian fragments and assorted basement rocks - from pyroclastic rim	East rim of crater 9138'	.968	.967	.971	.968	.969
F-66-14A	Q_m	Fragile crust of lacustrine silt and basaltic pyroclastics - unconsolidated	NE Paoha Is.	.968	.962	.965	.969	.968

TABLE 3 (cont'd)

INTEGRATED 8-14μ EMISSIVITIES OF ROCKS FROM MONO CRATERS REGION
(KERN-BUETTNER STYLE "EMISSIVITY BOX" - BARNES IT-3 INFRARED THERMOMETER)
MEASUREMENTS MADE AT INFRARED LABORATORY, U.S.G.S., ARLINGTON, VIRGINIA
by

David L. Daniels

Field #	Unit	Rock Description	Location	1	2	3	4	Average
338	Q_{yrc}	Rhyolite pumice-low density pumice with large vesicules and dark colored glass	South Coulee	.959	.981	.959	.966	.966
SF-66-19	Q_{pA}	Sand flat unconsolidated pyroclastics-rhyolite lapilli - ash deposit	East craters sand flat	.969	.968	.961	.962	.965
S-66-5	Q_b	Calcareous lake deposit-white carbonate coating on cemented rhyolite beach sand	South shore beach of Mono Lake	.964	.966	.962	.966	.965
F-66-3	Q_{bt}	Bishop Tuff-upper unit-tan, crystal-lithic rhyolite tuff - rough, heavily weathered	One mile SE of Aeolian Buttes	.960	.962	.960	.960	.961
340	Q_{yrp}	Rhyolite lapilli-rhyolite pumice and obsidian with basement rocks-same as #339 except higher obsidian content	East rim of crater 9138'	.958	.953	.963	.961	.959
335	Q_b	Rhyolite beach sand-sorted rhyolitic glass fragments	Beach-South shore Mono Lake	.954	.961	.964	.958	.958
F-66-17	Q_b	Fragile crust of lacustrine silt-unconsolidated beach deposit	Black Point (station #1)	.959	.957	.958	.953	.957
F-66-14B	Q_m	Greenish tuffaceous sandstone	Eastern Paoha Island	.952	.957	.954	.954	.954

TABLE 3 (cont'd)

INTEGRATED 8-14μ EMISSIVITIES OF ROCKS FROM MONO CRATERS REGION
(KERN-BUETINER STYLE "EMISSIVITY BOX" - BARNES IT-3 INFRARED THERMOMETER)
MEASUREMENTS MADE AT INFRARED LABORATORY, U.S.G.S., ARLINGTON, VIRGINIA
by

David L. Daniels

Field #	Unit	Rock Description	Location	1	2	3	4	Average
X-66-1	Q_{yrc}	Rhyolite-medium density-surface flat, smooth lightly weathered	South side North Crater	.953	.948	.949	.953	.951
F-66-7	Q_{jlb}	Olivine basalt-abundant plagioclase phenocrysts-red-black,dull,rough,weathered surface	One mile NW of June Lake Junction	.948	.950	.952	.955	.951
F-66-1	Q_{bt}	Bishop Tuff-upper unit-tan-violet, crystal lithic rhyolite tuff-rough,light weathering	1/2 mi. NW of Aeolian Buttes	.945	.949	.953	.951	.950
F-66-4	Q_{bt}	Bishop Tuff-lower welded unit-dense,tan, crystal-lithic,rhyolite tuff-rough,heavily weathered.	1 mi. south of Aeolian Buttes	.946	.946	.946	.950	.947
S-66-6	Q_m	Greenish tuffaceous sandstone	East side Paoha Island	.943	.943	.938	.947	.943
F-66-9	Q_{or}	Rhyolite-vitrophyric (Feldspar phenocrysts) gray-brown, heavily weathered surface	2000' NE of Punch Bowl	.953	.938	.943	.944	.943
F-66-8	Q_{or}	Rhyolite-vitrophyric (abundant 1/8" feldspar phenocrysts)-gray-brown,moderate weathering	2000' NE of Punch Bowl	.940	.942	.942	.942	.942
F-66-15	Q_{pvA}	Basalt - fine grained, finely vesicular-black, fairly fresh surface	NE quarter Paoha Island	.938	.939	.959	.932	.942
S-66-3B	Q_{am}	Andesite-large plagioclase phenocrysts,lithic inclusions,layered fine-grained groundmass-dull surface	2 miles NW of Crater Mtn.	.936	.942	.940	.949	.942

TABLE 3 (cont'd)

INTEGRATED 8-14μ EMISSIVITIES OF ROCKS FROM MONO CRATERS REGION
(KERN-BUETTNER STYLE "EMISSIVITY BOX" - BARNES IT-3 INFRARED THERMOMETER)
MEASUREMENTS MADE AT INFRARED LABORATORY, U.S.G.S., ARLINGTON, VIRGINIA

by

David L. Daniels

Field #	Unit	Rock Description	Location	1	2	3	4	Average
S-66-1B	Q_{yrc}	Rhyolite-medium density-surface flat, rough moderate weathering	South side North Crater	.939	.938	.938	.940	.939
F-66-5	Q_{jlb}	Olivine basalt-abundant plagioclase phenocrysts, rough, dull-black surface	1 mile NW of June Lake Junction	.940	.938	.940	.935	.938
S-66-1A	Q_{yrc}	Rhyolite-dense flow material-surface flat, rough,dark weathering	South side North Crater	.939	.944	.930	.934	.937
S-66-3A	Q_{am}	Andesite-plagioclase phenocrysts-lithic inclusions,layered fine-grained groundmass-smooth surface coating	2 miles NW of Crater Mtn.	.929	.936	.935	.947	.937
G-66-15	Q_{rb}	Rhyolite pumice-finely vesicular, medium density, blocky ejecta-flat,rough,weathered surface	Satellite cone,1 mi. SEof North Crater	.933	.934	.936	.934	.934
333	K_a	Medium-grained,biotite quartz monzonite	Aeolian Buttes	.931	.928	.933	.932	.931
F-66-11	Q_{jlb}	Olivine basalt-abundant plagioclase phenocrysts, rough,black,dull glossy surface	1 mile NW June Lake Junction	.926	.926	.933	.927	.928
G-66-27A	Q_{yrc}	Rhyolite-dense,grades into obsidian-flat smooth surface, relatively unweathered	North Coulee	.902	.913	.927	.913	.914

TABLE 3 (cont'd)

INTEGRATED 8-14μ EMISSIVITIES OF ROCKS FROM MONO CRATERS REGION
(KERN-BUETTNER STYLE "EMISSIVITY BOX" - BARNES IT-3 INFRARED THERMOMETER)
MEASUREMENTS MADE AT INFRARED LABORATORY, U.S.G.S., ARLINGTON, VIRGINIA
by

David L. Daniels

Field #	Unit	Rock Description	Location	1	2	3	4	Average
S-66-3C	Q_{am}	Andesite-large plagioclase phenocrysts, lithic inclusions, aphanitic groundmass-gray, dull, glossy surface	2 miles NW of Crater Mtn.	.916	.920	.895	.918	.912
G-66-2C	Q_{yrt}	Dark rhyolitic obsidian-dull, frosted fracture surface	Talus slope North Crater	.891	.890	.900	.904	.896
G-66-2A	Q_{yrt}	Grey-black rhyolite obsidian-smooth, glassy fracture surface	Talus slope North Crater	.868	.867	.870	.871	.869
G-66-2B	Q_{yrt}	Grey-black rhyolite obsidian-smooth, glassy fracture surface	Talus slope North Crater	.864	.868	.870	.870	.868

TABLE 4

RELATIONSHIP BETWEEN AMPLITUDE OF DIURNAL SURFACE TEMPERATURE CURVES AND THERMAL PARAMETERS FOR SELECTED LITHOLOGIES OF THE MONO AREA, JULY 27-28, 1966

Lithology	Amplitude of diurnal surface temp. curve July 27-28, 1966 °C	$F_o/_\beta$	Net radiant salor flux $F_o = J_o (1-r_o)$	Incident radiant flux (J_o)	Total reflectivity expressed in terms of absorption of solar radiation $1 - (r_o)$	Thermal inertia ($\beta = \sqrt{kpc}$) in c.g.s. units	Thermal conductivity (k)	Bulk density (ρ)	Thermal diffusivity (α)	Specific heat (C)	Integrated Emissivity ($\varepsilon_{\lambda\ 8\text{-}14\mu}$)
Qvb Basalt lapilli ash of Black Point	57±2°	0.462	0.017	0.0250	0.75	0.037**	0.004**	1.9?**	0.011**	0.2**	0.985± 0.003
QpA Q_b Rhyolite pumiceous sand of South Beach and pumice sand flats	51±1°	0.439	0.004	0.0250	0.2	0.009*	0.0006*	1.0*	0.004*	0.16*	0.958 ±0.006
Qbt Bishop tuff (upper unit) of Aeolian Buttes	50±2°	0.375	0.015	0.0250	0.6	0.040*	0.0028*	1.8*	0.0086	0.18*	0.947± 0.003

TABLE 4

RELATIONSHIP BETWEEN AMPLITUDE OF DIURNAL SURFACE TEMPERATURE CURVES AND THERMAL PARAMETERS FOR SELECTED LITHOLOGIES OF THE MONO AREA, JULY 27-28, 1966

Lithology	Amplitude of diurnal surface temp. curve July 27-28, 1966 °C	F_o/β	Net radiant solar flux $F_o = J_o(1-r_o)$	Incident radiant flux (J_o)	Total reflectivity expressed in terms of absorption of solar radiation (r_o)	Thermal inertia ($\beta = \sqrt{kpc}$) in c.g.s. units	Thermal conductivity (k)	Bulk density (ρ)	Thermal diffusivity (α)	Specific heat (c)	Integrated Emissivity ($\varepsilon_{\lambda 8-14\mu}$)
Qal Silty playa crust and deltaic deposits of Black Point	48±1°	0.427	0.011	0.0250	0.4	0.024*	0.0014*	1.8*	0.003*	0.24*	0.957 ± 0.004
Qm Lacustrine carbonate crust of Black Point	47±2°	0.423	0.005	0.0250	0.2	0.012**	0.0011**	1.8**	0.003*	0.2**	0.974 ±0.002
Q_b Lacustrine carbonate cementing pebbles of South Beach	36±1°	0.263	0.010	0.250	0.4	0.038**	0.004**	2.0**	0.011**	0.18**	0.965± 0.003

TABLE 4

RELATIONSHIP BETWEEN AMPLITUDE OF DIURNAL SURFACE TEMPERATURE CURVES
AND THERMAL PARAMETERS FOR SELECTED LITHOLOGIES OF THE MONO AREA, JULY 27-28, 1966

Lithology	Amplitude of diurnal surface temp. curve July 27-28, 1966 °C	F_o/β	Net radiant solar flux $F_o = J_o (1-r_o)$	Incident radiant flux (J_o)	Total reflectivity expressed in terms of absorption of solar radiation (r_o)	Thermal inertia ($\beta = \sqrt{kpc}$) in c.g.s. units	Thermal conductivity (k)	Bulk density (ρ)	Thermal diffusivity (α)	Specific heat (c)	Integrated Emissivity ($\varepsilon_{\lambda\ 8-14\mu}$)
K_a Quartz monzonite of Aeolian Buttes	28±2°	0.250	0.015	0.0250	0.6	0.060*	0.0075*	2.8*	0.017*	0.16*	0.931 ±0.003

2) From recorded surface temperature curves
3) Calculated from $T_o = Tmd + \frac{Fo}{\beta} f$
4) Calculated from $F_o = J_o (1-r_o)$
5) From recorded Epply pyrhetiometer curve
6) Estimated from diurnal temperature curve
7) *Approximately equal to USGS laboratory determinations by data cited in Clark, S. J., 1966, Handbook of Geophysical constants.
8) *Laboratory determinations
9) *Laboratory determinations
10) *Laboratory determinations
11) *Laboratory determinations
12) *Laboratory determinations

**Estimated from diurnal temperature curves
**Estimated
**Estimated
**Estimated
**Estimated

ACKNOWLEDGEMENTS

This study was carried out with the support of the staff of the Infrared Laboratory, Geological Survey, under the supervision of Robert M. Moxham, and with the cooperation of pilots, Raymond Rote and Howard Chapman flying the Geological Survey, Water Resources Division aircraft in which an infrared scanning radiometer and supporting equipment were mounted. Charles R. Fross operated the scanning radiometer with the assistance of Robert M. Turner. Philip W. Philbin and George R. Boynton set up ground monitoring instruments including an Epply pyrheliometer, variable sequencer thermistor systems, and Barnes IT-2 and IT-3 radiometers. Robert M. Turner processed the imagery. Joanne K. Oman and Philip W. Philbin operated the isodensitometer in the laboratory. David L. Daniels made laboratory emissivity determinations on rock samples collected from the Mono area and Gordon W. Greene provided data on thermal parameters of many of these same rocks. Roger Bowen, Branch of Computations, Geological Survey, Menlo Park, programmed the function given by Jaegar and Johnson for diurnal temperature variations. Alonzo E. Stoddard provided notes on infrared radiation theory, emissivity and absorptivity. G.G. Dalyrmple, C.W. Chesterman, C.H. Gray and Clyde Wahrhaftig contributed useful geologic information on the Mono area and David L. Daniels, Stephen J. Gawarecki, Gordon W. Greene and R.J.P. Lyon accompanied the author in the field on several occasions. Stephen J. Gawarecki kindly made available several photographs of Paoha Island for use in this report.

REFERENCES

1. Buettner, K. J. K., Kern, C. D., 1965, The determination of infrared emissivities of terrestrial surfaces: Jour. Geophys. Res., v. 70, no. 6, PP 1329-1337.

2. Brunt, D., 1932, Quart. Jour. Royal Met. Soc: 58, 389.

3. Butuzova, G. Yu., 1966, Iron-ore sediments of the fumarole field of Santorin Volcano, their composition and origin: Doklady Akademii Nauk SSSR, v. 168, no. 6, p. 1400-1404.

4. Carslaw, H. S., and Jaeger, J. C., 1959, Conduction of heat in solids: Oxford, Clarendon Press, 2 ed., SIOP.

5. Christensen, N. H., and Gilbert, V. M., 1964, Basaltic cone suggests constructional origin of some guyots: Science, v. 143, no. 3603, p. 240-243.

6. Friedman, J. D., 1967, Geologic map of the Mono Craters Area, California: Tech. Letter NASA-12, Geological Survey for the National Aeronautics and Space Administration.

7. Gouffé, André, 1945, Corrections douverture des corpsnoirs artificiels compte tenu des diffusions multiples internes: Rev. 'Optique, 24, No. 1-3, PP. 1-10.

8. Jaeger, J.C., and Johnson, C. H., 1953, Note on diurnal temperature variation: Geofisica Pura e Applicata, v. 24, Milano.

9. Pakiser, L. C., Press, F., and Kane, M. F., 1960, Geophysical investigation of Mono Basin, California: Geol. Soc. Amer. Bull., v. 71, no. 2 p. 153-160.

10. Russell, Issac, 1889, Quaternary history of Mono Valley, California: U. S. Geol. Survey, 8th Ann. Rept., 1887-1889, pt. 1, p. 261-394.

11. Scholl, D. W., von Huene, Roland, and St.-Amand, Pierre, 1966, Geology of Mono Lake: Geol. Soc. Sacremento, Guidebook along the East-Central Front of the Sierra Nevada, Ann. Field Trip, June 18-19, 1966.

For a list of pertinent reports on the geology of the Mono Craters area through 1965, see Friedman, J. D., 1967, Geologic Map of the Mono Craters Area, California: Technical Letter NASA-12, Geological Survey for the National Aeronautics and Space Administration.

Figure 27. Aerial photograph of Paoha Island showing areas scanned by isodensitracer technique. Arrows on east side indicate points of thermal emission.